CEA Saclay
Internal report: IRFU-09-109 - (2009)
EURISOL DS/Task#5
www.eurisol.org

LAY-OUT OF THE EURISOL POSTACCELERATOR

D. Ene, J. C. David, D. Doré, D. Ridikas
CEA-Saclay, IRFU / Service de Physique Nucléaire, 91191 Gif-sur-Yvette

Abstract

This report summarises the radiation protection studies conducted for the EURISOL post accelerator. The goals of the work were to study the important radiological aspects of the post-accelerator layout, to make pre-conceptual designs for the most important items including the tunnel, the beam dump and experimental area, to characterize the radiation environment through over the installation and its impact on the EURISOL facility, and to identify further required analyses.

PHITS1.94 Monte Carlo code simulations, complemented by DCHAIN SP-2001 transmutation program calculations were performed to evaluate the necessary shielding walls, to estimate the radiological impact of the accelerator items and to calculate the radioactivity in the air and in the components of the incorporated devices. Monte Carlo simulations by means of the beta version MCNPX2.6.e code were performed also in order to build confidence in the PHITS estimates.

Two possible variants of linac lay-outs: i) without stripper (L#1) and ii) with stripper (L#2) were analyzed using the $^{132}Sn^{25+}$ radioactive beam of unprecedented intensity, namely up to ~10^{13} pps, as reference for simulations. Emphasis was laid upon estimating the shield concrete walls of the tunnel that lowers the dose rates to acceptable levels for operation personnel and/or environment. Dose profiles after shut-down of the facility based on normal operation beam losses were also estimated at the extremities of the accelerator tunnel.

A preliminary concept of the beam dump required to provide safe operation conditions of the post-accelerator was further developed. In addition to the energy deposit calculations, material activation estimates have been carried out for all materials in the dump. The lateral shielding thicknesses for the beam dump cavity were derived for two candidate materials, iron and ordinary concrete.

The configuration of the shielding and the management of the access to the controlled areas inside the beam experimental hall were studied using a simplified experimental set-up. This geometry model contains a) a simplified AGATA detector placed in the centre, b) a typical experimental target positioned inside AGATA, and c) the same beam dump concept previously used for the final stop of the ion beam delivered by post-accelerator. The experimental target configuration was selected via an initial investigation over six target materials: CH_2, Be, C, Cu, Ni and Pb at two possible thicknesses of 1 mg cm^{-2} and 10 mg cm^{-2}.

Future work will be required to develop a more detailed concept for the post-accelerator area based on the results obtained here.

INTRODUCTION

The great success of the present radioactive ion beam (RIB) facilities is a strong motivation to plan new generation of large-scale ISOL (Isotope Separation On-Line) facilities. EURISOL DS, see (www.eurisol.org), is the European common effort in planning a next generation RIB facility able to deliver secondary beams of 10^{13} pps at energies up to 150 MeV u^{-1}, exceeding thus by at least a factor 100 the ion yields delivered by the current facilities or those under construction.

The intense beam as well as the accessibility to heavier nuclear systems will provide many new opportunities permitting to investigate more exotic regions of the nuclear chart, unreachable to date. More than 25 key experiments envisaged in the science case of EURISOL, see (www.eurisol.org), will address important fundamental physics topics: nuclear structure, nuclear reactions, nuclear astrophysics, and fundamental interactions including the tests of the standard model.

The proposed schematic layout of the facility contains: a high-energy high-intensity proton driver accelerator, several target ion-source (TIS) systems, a mass-separator and a post-accelerator. The unprecedented increase of the RIB intensities will give rise to challenging issues in terms of nuclear safety and radioprotection.

In the framework of the radiation characterization and safety studies within Task 5 see (Ridikas et al., 2007) detailed calculations were performed to characterize the radiation environment and design the appropriate shielding along the entire EURISOL facility.

It is critical to know since the early stage of the design the prompt radiation levels that drive bulk shielding requirements, radiological inventories, radiological environmental impact, activation levels of materials surrounding regions of beam loss, estimation of doses to radiation workers and remote maintenance requirements.

The purpose of these preliminary safety studies carried-out within the Task#5 of the EURISOL Design Project is to design the appropriate shielding and to characterize the residual field in the post-accelerator tunnel and its surroundings.

Dedicated simulations were performed by means of the PHITS1.94 code (Iwase, 2002). Monte Carlo simulations by means of the beta version MCNPX2.6.e code (James et al., 2006) were performed also in order to build confidence in the PHITS estimates for the EURISOL post-accelerator shielding. Two benchmark problems addressing the heavy ion interactions at intermediate energies were used to test the physics models of these codes. Both physics models used show an overall good agreement with the experimental data. Additional comparisons have been performed to validate the results of simulations using the reaction induced by ^{132}Sn at 150 MeV u^{-1} on copper, being the reference reaction in our design calculations.

The induced radioactivities in all analyzed items: accelerator tunnel, beam dump cavity and the experimental hall were estimated using DCHAIN-SP-2001 code (Kay et al., 2001) based on external neutron source and spallation products derived from PHITS. Ambient dose equivalent rates due to the residual radiation were calculated with the MCNPX code using photon sources resulted from DCHAIN. The effect of implanted radioactive ions at low energies in accelerator structure was also assessed.

The report is organized in the following way.

The first chapter reports the studies performed to obtain radioactive doses and levels of activation inside the accelerator tunnel.

There are two options available for the extracted and ionized RIBs from the ISOL targets in combination with the linear post-accelerator: i) the beam is transmitted in the absence of any strippers (L#1) and ii) one stripping station is foreseen along the accelerator (L#2). Both variants of the linear post-accelerator lay-outs were analyzed using the $^{132}Sn^{25+}$ radioactive beam at its intensity of ~10^{13} pps as reference for our simulations.

In this respect simulations were done to address major shielding requirements impacting civil construction and environmental protection. First facility radiation field overviews were also performed to obtain levels of activation and radioactive doses.

The second part of the report describes the preliminary concept of the beam dump required to provide safe operation conditions of the post-accelerator. A V-shaped dump configuration having a water-cooled graphite core was investigated in this study. The analysis shows that this conceptual model might be able to absorb within sufficient margin the beam power of the order of 20 kW. In addition to the energy deposit calculations, material activation estimates have been carried out for all materials in the dump. The report provides also the preliminary results of the lateral shielding requirements for the beam dump cavity.

The report ends up with the configuration of the shielding and the management of the access to the controlled areas inside the beam experimental halls. For this purpose a simplified experimental set-up was used in simulations. This geometry model contains a) a simplified AGATA detector placed in the centre, b) a typical experimental target positioned inside AGATA, and c) the same beam dump concept previously used for the final stop of the ion beam delivered by post-accelerator. The experimental target configuration was selected via an initial investigation over six target materials: CH_2, Be, C, Cu, Ni and Pb at two possible thicknesses of 1 mg cm^{-2} and 10 mg cm^{-2}. As previously, a test case of $^{132}Sn^{25+}$ RIB at 150 MeV $u^{-1}$was used in simulations.

The Annex provides detailed presentation of the obtained results and discussion on building confidence and assessing the validity of the computer codes used in evaluations.

1. POSTACCELERATOR TUNNEL

2.1. Calculation procedure.

2.1.1. Design requirements.

Radiation limits imposed to comply with in the shielding design are defined by the national legislation of each country. As the EURISOL facility site was not yet decided these constraints were fixed in accordance with ICRP 60 recommendations (ICRP 60, 1990).

The dose equivalent rate limit for normal operation was taken 0.1 μSv h^{-1} for public areas and 10 μSv h^{-1} for controlled areas. These values ensure that the annual dose equivalent limit of 1mSv for the public and 20 mSv limit for the workers for an operation time of 2000 h y^{-1} will not be exceeded. A shielding design is proposed for each classified area mentioned above.

An accident scenario considers a full beam loss ($6*10^{12}$ ions s^{-1}) at a single point that corresponds to a maximum loss of the 20 kW beam (150 MeV u^{-1}). The design requirement for a full beam loss used in CERN (Agosteo and Silari, 2001) states that a full beam loss at a localized point must not give rise to a dose equivalent rate outside the shielding higher than 100 mSv h^{-1} ensuring that the accelerator control system is able to abort the beam in a time given rise to an integral dose that remains under permissible limit for any worker. In this stage such safe limit was fixed to 50 Sv in accordance with the regulations of the majority of countries involved in the EURISOL project.

2.1.2. Radiation sources.

In the work two situations were analyzed for the shielding calculations: i) normal linac operation and ii) accidental full beam loss. At the time being no possible hot spots along the linac were specified in the design. For beam losses during routine operation the designers of the accelerator have provided two guideline values: 10^{-5} m^{-1} and 10^{-4} m^{-1}. These values correspond to beam losses of $6*10^{7}$ and respectively $6*10^{8}$ ions per meter and per second. According with the beam losses during operation should keep the induced radioactivity in the machine at a level sufficiently low to permit hands-on maintenance. Until reliable information will be available it was decided to study both assumed routine loss scenarios considering that the analysis of their consequences might indicate valuable information for feedback measures or even the rejection of one of it if it will be found prohibit.

In case of L#2 variant the design specification of 60% beam loss lasting along 5 m of the stripper zone was extended to the entire length of this station as no information is available up to date about losses in the downstream part of this item.

2.1.3. Design assumptions.

The strategy to design the radiation shield for the linac was based on two assumptions.

Firstly, in agreement with (Fasso et al., 1990) the uniform loss over a distance of about 10 m was assumed approximately equivalent with constant loss concentrated at a single point having 10 times more intensity. Thus the beam losses during operation were represented by point losses concentrated at defined position along the machine of $6*10^{8}$ ion s^{-1} in case of the beam loss scenario 1 (BLS#1) and respectively $6*10^{9}$ ion s^{-1} for the second beam loss scenario (BLS#2).

Even though the calculations were performed for both mentioned above scenarios the method and the most part of the derived results presented here refer to BLS#2. Therefore to facilitate the discussion the obtained results are presented without this specification. Based on this first hypothesis a simple geometry model was used to estimate the lateral shielding required for linac,

see details in chapter 3.1.1. PHITS Monte Carlo code version 1.94 was used to simulate the ^{132}Sn ion transport and calculate the equivalent dose rates spatial distributions H*(10) in the specified shield geometry. The resulted neutron attenuation curves in concrete were fitted by a double-exponential function, approach developed in (Agosteo and Nakamura, 2004) for transmission of secondary neutrons generated by heavy ions of intermediate energies.

Given beam power and energy the equivalent dose rate H*(10) was approximated by the following attenuation formula:

$$H(\theta, d/\lambda) = \frac{H_1(\theta)}{r^2}\exp\left(\frac{-d}{\Lambda_{1,\theta}}\right) + \frac{H_2(\theta)}{r^2}\exp\left(\frac{-d}{\Lambda_{2,\theta}}\right) \quad (1)$$

where r and θ are the spherical coordinates of the current point where the dose rate is measured and d is the total distance traversed by the radiation in the shielding material. H_1 and $\Lambda_{1,\theta}$ are the source term and the attenuation length of the low-depth exponential function describing the neutron behavior at the entrance in the concrete while H_2 and $\Lambda_{2,\theta}$ are the same parameters for the large-depth exponential function which model the equilibrium status reached.

Making use of Eq.1 the mentioned above parameters were fitted (θ = 90^o) for subsequent determination of the shield thickness needed to attenuate the radiation dose by the desired factor.

The second basic assumption adopted for the shielding design of the proton linacs see (Agosteo and Silari, 2001) states that a shield designed for a continuous loss during the routine operation is also adequate for an accident loss of a full beam at a localized point providing that the linac cut-off time is short enough to produce an integrated dose below the acceptable limit. Consistent with the above assumption the estimation of the lateral shielding of the linac is illustrated in the Fig. 1.

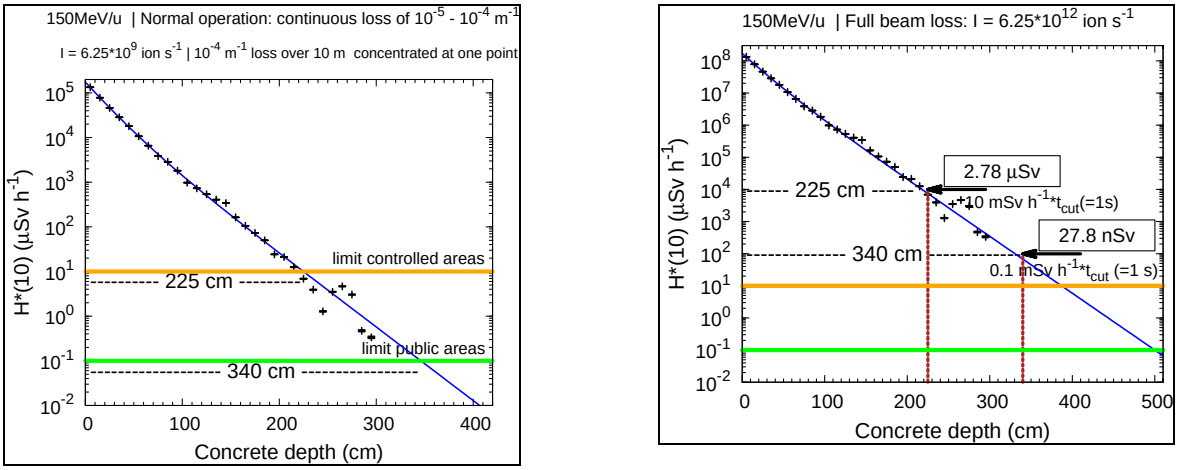

Figure 1: Neutron dose rate attenuation curves in concrete wall of the linac tunnel corresponding to 150 MeV u^{-1} ion beam energy (left) and full beam loss (right). Derived concrete thicknesses required to meet the design constraints are included to demonstrate that the expected integrated equivalent dose from full beam loss outside the predicted shields complies with the limits in case of a cut-off time of 1 s. With points is represented resulted PHITS attenuation profile while the continuous line is the curve fitted using the analytical formulation.

2.1.4. Design approach.

In the Fig.1 the resulted PHITS attenuation profile was processed from the scored 3D dose rate per incident ion matrix for an axial cross-section plan at 3 m from the loss point see details in the chapter 3.1.3. The appropriate scaling factor was further used to derive each of the two beam loss cases. The estimated parameters of the fit are given in the Table 1.

Applying the mentioned above method in case of 21 MeV u^{-1} ion energy beam that correspond to the first exit to experimental hall one can conceive the most conservative Linac shielding design made from two blocks each sized to sustain the maximum beam loss. However according with the ALARA principle it is desirable to minimize the shielding thicknesses. To answer at this requirement besides the experimental exits three more beam losses simulations along the accelerator were further investigated.

The corresponding energy values of these additional cases of 45.5, 76 and 115 MeV u^{-1} were chosen so that the tunnel of L #1 variant is divided in lengths of about 40 cm. Results of simulations fitted using Eq.1 can be described with the parameters in the Table 1.

It is apparent from the Table that mass attenuation length is increasing with the energy.

Table 1: Fitted parameters of the attenuation curves in concrete (H_0 = un-normalized source term and $\lambda = \rho * \Lambda$, ρ = mass density)

Energy [MeV u^{-1}]	H_{01} [Sv m^{-2} ion^{-1}]	λ_1 [g cm^{-2}]	H_{02} [Sv m^{-2} ion^{-1}]	λ_2 [g cm^{-2}]
150	$2.00*10^{-10}$	38.78	$7.98*10^{-11}$	62.00
115	$1.13*10^{-10}$	23.50	$6.14*10^{-11}$	57.32
76	$6.18*10^{-11}$	21.36	$1.27*10^{-11}$	53.20
45.5	$1.69*10^{-11}$	12.19	$1.55*10^{-11}$	40.52
21	-	-	$2.00*10^{-12}$	33.57

The lost beam inside the tunnel is considered constant in case of each accounted linac variants whereas the power of the beam increases progressively with the beam energy. The detailed design of the individual linac was derived following the strategy, synthetically represented in the Fig. 2.

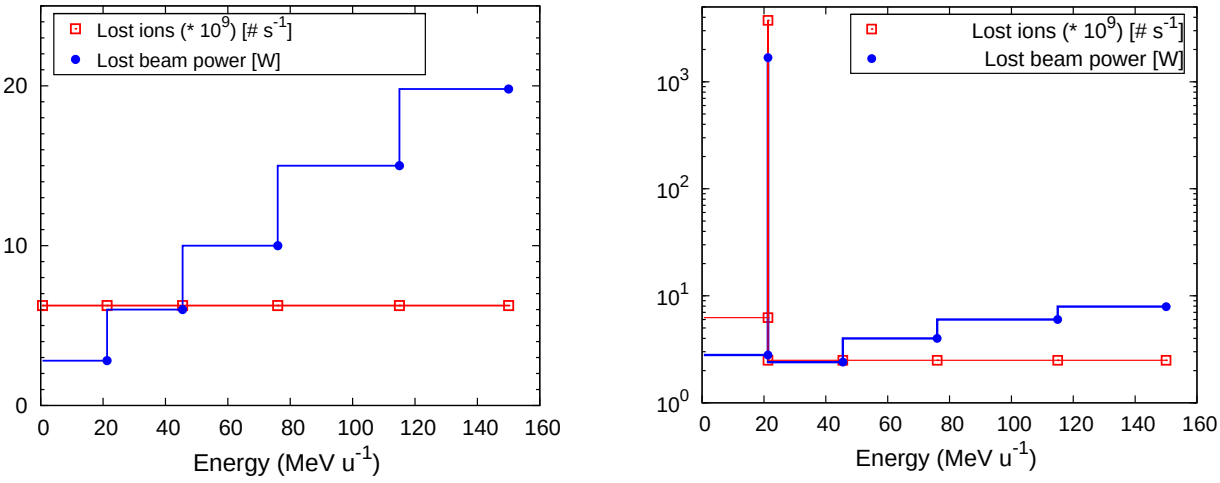

Figure 2: Strategy used in simulations: for linac variant L #1 (left) and L #2 (right) variant.

In the figure the lost beam power histogram defines the intervals chosen to model conservatively the shield blocks while the lost ions give the beam intensity scaling factors. It should takes notice of the fact that for L #2 variant were used the same lost power positions as for L #1 and consequently these points on the energetic scale delimitate different intervals along the linac length in accordance with the energy gradient curve of this machine.

As shown in this scheme as a consequence of the 60% beam loss in the stripper zone the corresponding beam power increases dramatically reaching almost 2 kW and consequently the lost ions and the lost power along to the accelerator downstream to this station drop relative to L #1 with the remaining complementary percentage.

2.2. Description of the simulations

2.2.1. Prompt radiation simulation

2.2.1.1. Geometry model.

A simplified geometry was adopted. The detailed geometry of the facility will be modeled in the more advanced stage of the project.

The lost ions were assumed to strike a thick copper target (5 X 5 X 5) cm^3 that approximates the copper structure of the quadrupoles or the cavity. A parallelepiped concrete shell with cross section of (300 X 300) cm^2 having 300 cm thickness was used to simulate the tunnel walls. The beam axis was placed asymmetrically (100 cm from one side) inside the tunnel. A soil 100 cm thick layer was placed outside the tunnel concrete walls. The total length of the shielding structure was set to 10 m what was found a good pattern for the developing of the nuclear cascade.

Compositional data, nuclide content and impurity elements present within the component materials have been chosen as follows:

i. GLIDCOP Al-25 (ρ = 8.85 g cm^{-3}) for Cu target see (Cepraga, 2008): Cu 99.49 %, Al 0.25 %, O 0.22 %, B 0.025 %, Se 0.003 %, Fe 0.002 %, Te 0.002 %, S 0.001 %, Zn 0.001 %, Sb 0.001 %, As 0.001 %, Pb 0.001 %, Sn 0.0009 %, Mn 0.0002 %, P 0.0002 %, Bi 0.0002 %, Cd 0.0001 %;

ii. ordinary concrete (ρ = 2.3 g cm^{-3}) chemical composition of the research reactor ULYSSE CEA Saclay (Aubert, 2005): O 52.9%, Si 21.8%, Ca 17.4%, C 3.7%, Al 1.5%, Fe 1%, K 0.5%, H 0.4%, Na 0.4%, Mg 0.3%, S 0.1% and other more than 70 traces up to Uranium;

iii. Air inside the tunnel (ρ = 1.24375*10^{-3} g cm^{-3}): N 75.558 %, O 23.159 % and Ar 1.283 %;

iv. Soil surrounding the tunnel, a composition (ρ = 1.6 g cm^{-3}) derived from several soil-samples from Krauthausen location (North Rhine-Westphalia) see (Schlogl, 2007): O 50.1 %, Si 37.3 %, Ti 9.7 %, Fe 1.5 %, K 0.9 %, Al 0.4 %, Zn, Pb, Mn, P, Cr, Ni, Cu each less than 0.1 %. Ground water composition used in calculations was taken from same reference.

2.2.1.2. Physics model.

PHITS code uses an intranuclear cascade model to simulate nucleon-induced reactions and a model based on QMD theory for reactions induced by both nucleons and heavy ions. Statistical decay of compound nucleus is calculated with GEM (Furihata, 2001) an extension of the DRESNER evaporation model. Benchmark studies against available experimental data were performed initially (see Annex) in order to verify the accurate description of the reaction models used in the code and to decide on the best options to be used for the present work requirements.

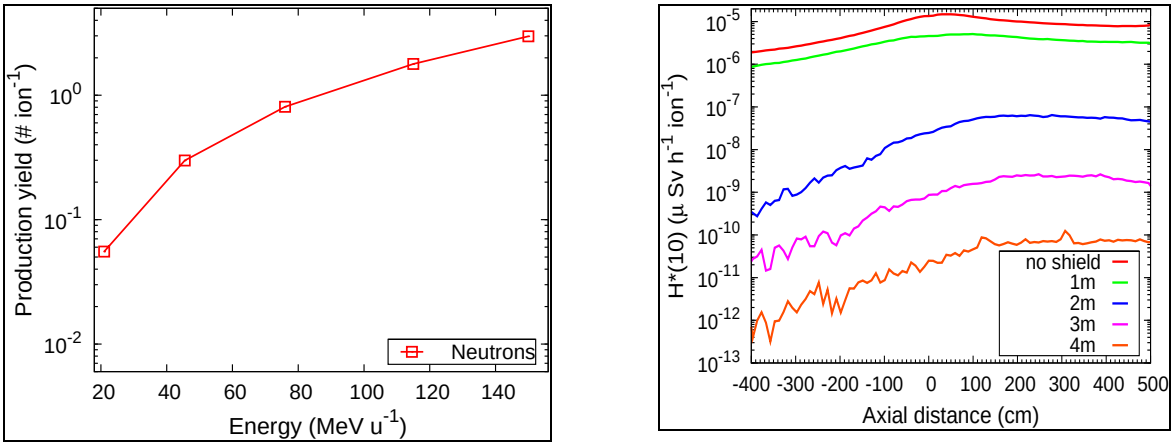

Figure 3: Neutron production yield as a function of the ion energies considered in this work (left). Axial distribution of H(10) in concrete shield at various distances from the beam axis (right).*

The good capability of the code to predict neutron spectra from thick targets bombarded with heavy ions from He to Xe in the intermediate range energy between 400 to 800 MeV u^{-1} was also recently demonstrated in (Satoh, 2007). All these data indicate that the PHITS QMD model is able to give a proper evaluation of the secondary neutron spectrum produced in a medium by heavy-ion bombardments within the energy range of interest around 100 MeV u^{-1}.

The axial distributions of the dose equivalent rates at several depths in the concrete are shown in the right panel of the Figure 3. It is apparent from the figure that the curves are biased in the forward direction showing the cascade developing. The peak laying at around 3 m from the beam impact with the target is better observable with the thickness increasing of the concrete wall. Therefore to be on the safer side all the results presented in this paper are referring to the axial location z = 3 m from the target.

The different treatment used to fit the neutron attenuation curve for 21 MeV u^{-1} tin ions on copper from the Table 1 is justified by observing neutron spectral fluencies distributions in the concrete depths given in the Fig.4. The high-energy peak around 80 - 90 MeV as well as the isotropic evaporation component centered at around 3 MeV that characterized neutron emission from the target are displayed for 150 MeV u^{-1} energy. The slight shift towards higher energies with larger depths shows the two-phase feature of the attenuation curves that was approached by the double exponential Eq.1.

In the concrete low-depths the low energy neutrons are attenuated with a short attenuation length producing the sharp slope in the beginning of the curve. Further, in the large-depths the remaining hard neutron component is reaching the equilibrium that is characterized by a larger attenuation length.

These trends are not present for the low energy case where a broad peak around few MeV is observed and the quasi-equilibrium seems to be reached since the entrance in the concrete.

The influence of other secondary particles produced in interactions with linac structure and concrete shield was investigated for 150 MeV u^{-1} and it was found that their contribution to the total H*(10) is negligible. For instant the ratio of H*(10) induced by photons to the total H*(10) is less than 3% showing that the neutrons are the dominant in the shielding estimates.

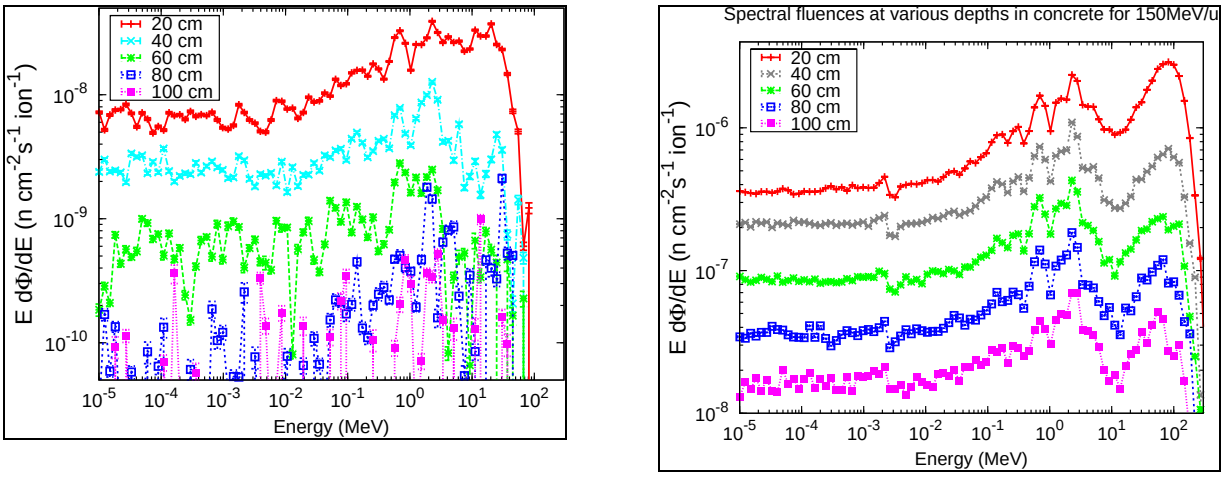

Figure 4: Neutron spectral fluences at various depths in concrete, for lost ions of 21 Me V u^{-1} (left) and 150 MeV u^{-1} (right).

2.2.1.3. Simulation technique

The splitting/importance variance technique was used for the PHITS simulations based on the geometry model described in chapter 3.1.1. The nuclear data library underlying all present simulations is based mainly on the ENDF/B VII evaluated file.

2.2.2. Residual radiation simulation

For activation analysis PHITS was coupled with DCHAIN-SP that is using FENDL/A-2 based activation data set together with FENDL/D-1 and ENSDF decay data libraries. It calculates the nuclide inventory, radioactivity, decay heat and gamma-ray energy spectra being able to read directly the distribution of the residual nuclei produced by PHITS code.

The radioactivity in the air was estimated using PHITS code option that allows the folding of particle track-length spectra with evaluated isotope production cross sections. The code contains a database with evaluated neutron and proton interaction cross sections of alpha, ^{14}N, ^{16}O targets cases that is used for the conversion of the air constituents into the radionuclides of interest.

MCNPX photon transport simulations were further carried out to estimate the ambient dose equivalent rates at surface and at one meter distance from the irradiated element.

DCHAIN derived photon source implemented in the MCNPX modeling were defined in VITAMIN-J library energy group structure. ANSI/ANS-6.1.1-1977 conversion factors to obtain the biological equivalent dose response function were employed.

In order to account for the accumulation effect, see (Sullivan, 1992), an operation history covering 1 year with alternated time sequences of 3 weeks of beam followed by 3 weeks of cooling was used in calculations. Only for the air activation an operation campaign of 12 days was accounted. Subsequent cooling times up to 10 years after irradiation period were assumed.

Dose rates were determined for different decay times until six months for the two extreme segments of the tunnel: i) low energy zone (21 MeV u^{-1}) and ii) high energy zone (150 MeV u^{-1}).

A crude approach has been used to model the beam implantation on the accelerator structure: it was considered that full beam is implanted in a point.

2.3. Results and discussion

Preliminary safety analysis of the results obtained using the most conservative assumptions conducts to the following results.

2.3.1. Shielding configurations

The minimum derived shielding thicknesses required to reduce the ambient dose equivalent below the public limit and below the design value of a controlled radiation area are given in Figure 5 and Table.2.

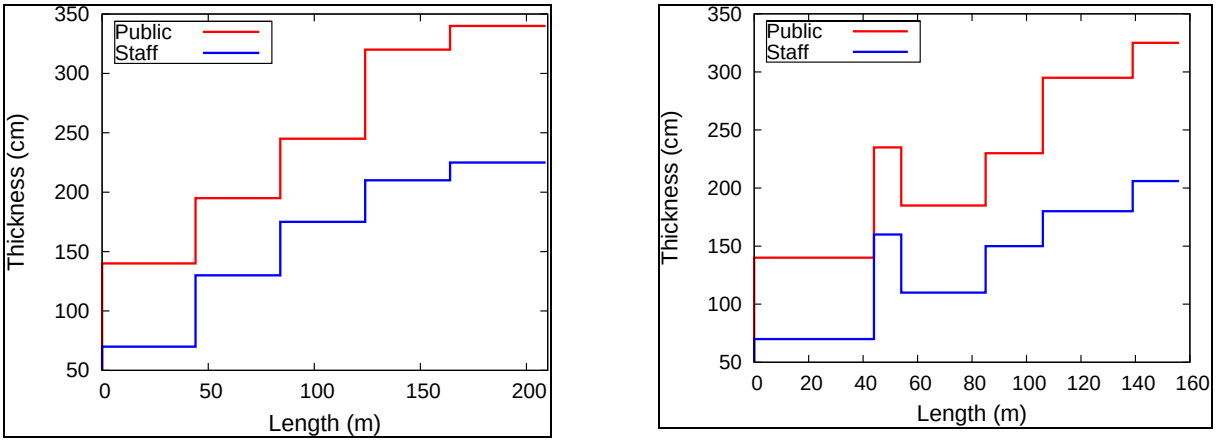

Figure 5: Thickness of the shielding blocks along the beam axis required to reduce the dose equivalent rate below 0.1 µSvh^{-1} (the limit for public exposure) and 10 µSvh^{-1} (controlled radiation area) for L#1 on the left and for L#2 on the right.

Table 2: Size of the shielding blocks required to reduce the dose equivalent rate below 0.1 µSv h^{-1} (the limit for public exposure) and 10 µSv h^{-1} (controlled radiation area) for BLS#2.

Shield block	L#1			L#2		
	Length (cm)	Thickness [m]		Length (cm)	Thickness [m]	
		Public	Staff		Public	Staff
21	44	140	70	44	140	70
Stripper zone	-	-	-	10	235	160
45.5	40	195	130	31	185	110
76	40	245	175	21	230	150
115	40	320	210	33	295	180
150	45	380	225	17	325	200
Volume* [cm^3]		536.6	338.05		343.4	205.8

* Correspond to a width = 1m

The proposed thicknesses of the shielding guarantee an integrated dose in case of accident below the acceptable limit with sufficient margin to cut off the beam in 1 s.

In the stripper zone the estimated shield thickness is thinner compare to that for 150 MeV u^{-1}

due to the small attenuation length value at low energy (see Table 1) that compensates the high beam loss. For the L#1 case the public required shield thicknesses can be reported as 13*λ (λ the mean free path at equilibrium from the Table 1) for blocks corresponding to 115 and 150 MeV u^{-1}, about 11* λ for energies of 45.5 and 76 MeV u^{-1} and 10* λ at 21 MeV u^{-1}. While for the shields needed for controlled area a scaling factor of 1.5 can be applied to mention above ratios for all energies but 21 MeV u^{-1} where the difference is a factor 2.

From the shielding safety point of view L#2 is a more advantageous variant as it requires only 61-64% from the shielding necessary for L#1. Placing the linac in a designated controlled area (dose below 10 μSv h^{-1}) might reduce the total shielding with 40%.

Prompt radiation of other ion species has an important impact on the shielding sizing. Calculations shown that in case of $^{6}He^{2+}$ acceleration at 250 MeV the equivalent dose rate past the shielding wall is five times higher compared to the reference case described above**.** Therefore complex simulations has to be performed to ensure universal conditions for all exotic nuclear beam experiments to be planned at the facility and to establish a well-defined safety operation domain: allowed energy range and beam intensities.

2.3.2. Residual field inside the tunnel

Activation data are provided in the Figure 6 as specific total activities at ion energies under study. For high energy the dominant nuclides representing more than 80 % from the total activity are shown also. In comparison with the preliminary results from (Ene, 2008) where only 12 days of irradiation was analyzed the present results are roughly the same for short times (few hours) from the beam switched off due the saturation of the short living nuclides, but at longer cooling times the irradiation period becomes more important and the ratio between results reflect the irradiation time ratio between the two scenarios.

High total activation value of approximate $5.2*10^{6}$ Bq cm^{-3} coming from accelerator structure at 1 hour decay time is due to $^{64,62,61,65}Cu$ radionuclides while at long times ^{59}Fe ,^{60}Co, ^{3}H and ^{63}Ni are dominants. The main contributor as short times is ^{64}Cu produced from thermal neutron capture in ^{63}Cu (high activation cross section of 4.5 barn). Contribution of the tunnel concrete wall to the total activity and consequently to the H*(10) is not significant. Concrete contains 0.4% of sodium which results in thermal neutron produced ^{24}Na, being the major contributor to the dose rates near the walls shortly after the beam is switched off.

The ^{37}Ar isotope issuing from Ca activation dominates the concrete activity until almost 6 months while for longer decay time ^{3}H and further ^{238}U together its ascendants become majority giving rise nevertheless to a small activity value. The decay time distribution of the specific activity in concrete depth until 100 cm with layers of 20 cm thickness scales approximately as the energy dependence depicted in the left-middle panel of the Fig.6 for the inner wall stratum.
^{41}Ar and ^{11}C are the main short lived radionuclides produced in the air given rise to a total activation of 0.35 Bq cm^{-3} at the operation shut-down time, while for longer decay times ^{7}Be is dominant. The concentrations of the radioactivities in the air have to be compared to regulatory limits for purposes of limiting worker doses. If one compare for instance the resulted specific activity of ^{41}Ar with the derived air concentration (DAC) value of ^{41}Ar of 0.5 m Bq cm^{-3} taken from 10 CFR part 385 (cfr.vlex.com/vid/835-concentrations-dac-controlling-19618720) one can see that overtakes with almost one order of magnitude. The 10 CFR DAC values are based on either a stochastic (committed effective dose equivalent) dose limit of 0.05 Sv or a non-stochastic (organ) dose limit of 0.5 Sv per year, whichever is more limiting.

The obtained estimates of the concentration of the radioactivity in air may be used to derive the air change rate inside the entire tunnel volume.

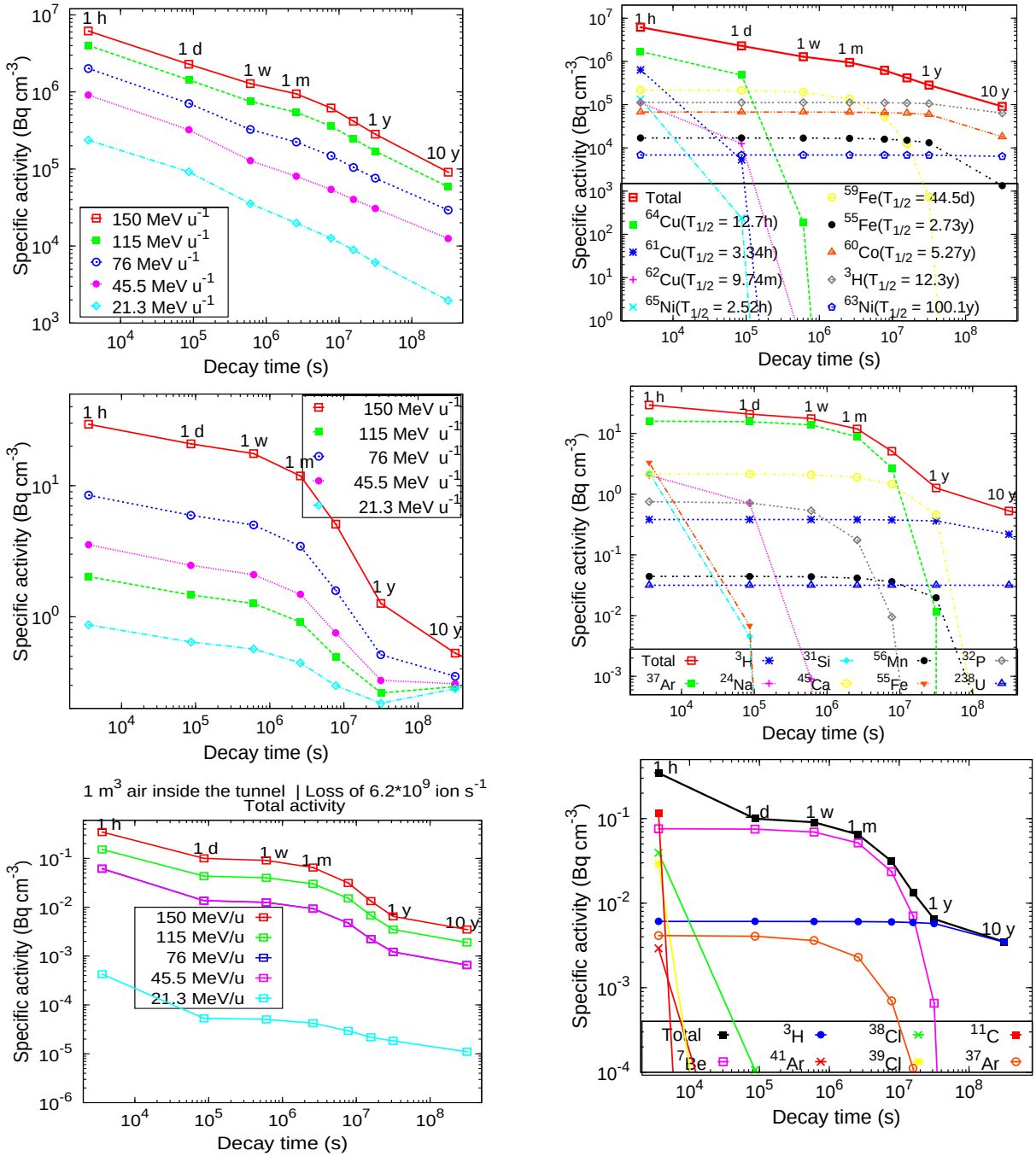

Figure 6: Obtained specific activity distributions versus decay time: total activity for accounted ion energies (left) and dominant radionuclides produced in case of the lost ions of 150 MeV u^{-1} energy (right). From top to bottom the results correspond to: the copper target, the inner 20 cm layer of concrete, 1 m^3 of air inside the tunnel

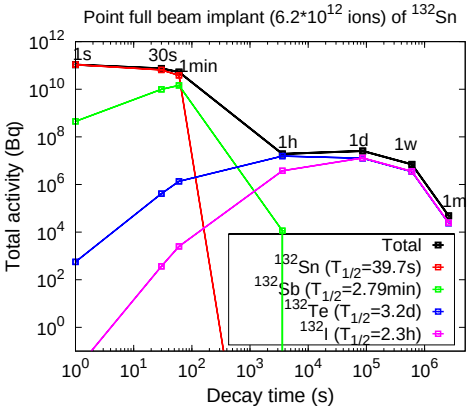

Figure 7: Total activity due to implantation

Consequently to the conservative assumption accounted high radioactivity value of more than 10^{11} Bq originating from ^{132}Sn implantation was found (see Fig.7). Accumulation of the daughter ^{132}I nuclide starting with 1 hour decay period increases considerably the potential hazard inside the tunnel

.

Predicted activities and dose rates after activation are given in the Fig. 8

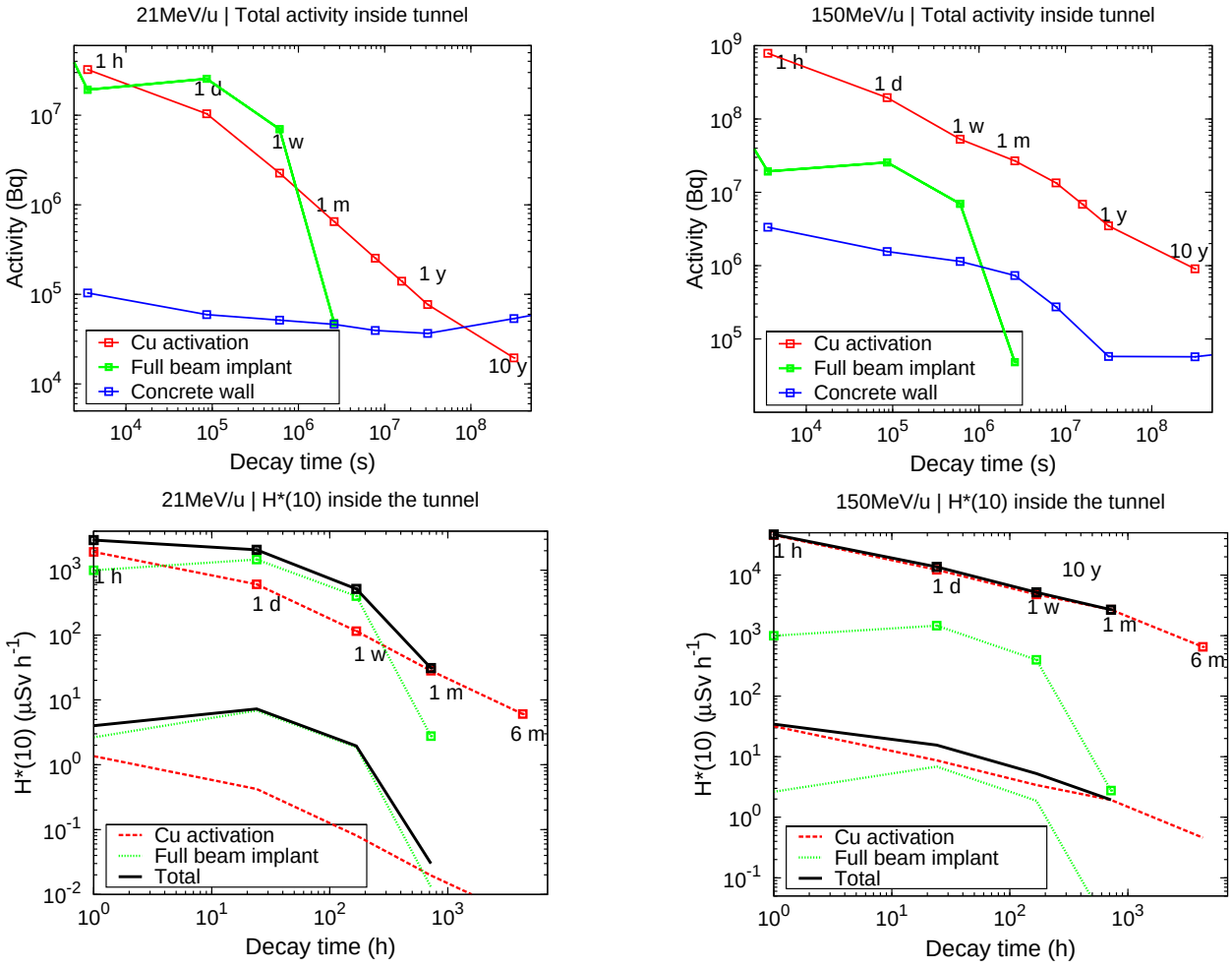

Figure 8: Estimates of the residual field inside the tunnel for the low energy zone (left) and for the high energy zone (right). On the top the results correspond to the total activities and on the bottom to the corresponding dose rates. Contact H(10) estimates are represented with points while lines refer to the results at one metre distance.*

Residual activation field inside the tunnel are arising mainly from copper structure activation in the high energy zone of the accelerator, while in the accelerator low energy zone the ion implantation is the most significant contributor.

In the high energy zone of the linac continuous accessibility inside the tunnel in the beam-off stage is possible only after one week cooling time. If intervention is required previously an occupancy factor of minimum 570 hours per year allows to meet the constraint of 20 mSv y^{-1}.

Contact dose rate values significantly higher than the limits show that a remote handling of the dismantled component is necessary. For the item extracted from the accelerator structure in the high energy zone even after one month cooling time the contact dose is higher than 1 mSv h^{-1}.

Definition of the intervention is required. To protect the personnel during the handling operations the access and transportation paths should be set-up and a hot cell might be necessary to be included in the facility lay-out.

Corroborating all results one can conclude that:

- Analysis of the possibilities to reduce the shield thicknesses has to be done;
- Maintenance operations inside the tunnel have to be planned;
- Design of a ventilation system in the tunnel is necessary;
- Several equipments and material should to be disposed of as radioactive wastes.

2.3.3. Source term for contaminant transport.

The standard deviation for the flux determination in the soil beyond 3 m of concrete wall was less than 20%. The results for the ten most important isotopes from the point of view of the environmental risk assessment (Thomas and Stevenson, 1988) are shown in the Table 3. Calculations have shown that most of these radionuclides are produced by spallation.

Exposure periods of one year and 40 years of continuous operation with a duty factor of 0.7 were used for the activation analysis.

Table 3: Specific activity [Bq cm^{-3}] in first 100 cm of soil/ground water surrounding the concrete wall after 40 years of continuous irradiation.

Isotope	$T_{1/2}$	Soil	Ground water
^{3}H	***12.33 y***	***$3.149*10^{-5}$***	***$3.299*10^{-6}$***
^{7}Be	53.12 d	3.662*10-6	$3.662*10^{-7}$
^{22}Na	***2.60 y***	***$7.782*10^{-6}$***	***$7.784*10^{-7}$***
^{24}Na	14.96 h	$7.551*10^{-6}$	$7.583*10^{-7}$
^{32}P	14.26 d	$1.047*10^{-8}$	$9.584*10^{-9}$
^{35}S	87.32 d	$2.262*10^{-23}$	$4.938*10^{-9}$
^{45}Ca	162.61 d	$8.111*10^{-6}$	$7.800*10^{-7}$
^{46}Sc	83.79 d	$6.833*10^{-7}$	$2.540*10^{-21}$
^{54}Mn	312.3 d	$2.217*10^{-7}$	$3.674*10^{-13}$
^{55}Fe	2.73 y	$2.679*10^{-6}$	$4.912*10^{-12}$
^{65}Zn	244.26 d	$3.867*10^{-8}$	$5.880*10^{-12}$

The source term presented in the table above is submitted for a subsequent detailed environmental assessment study. A rough examination of the obtained results draws to the conclusion that with a concrete shield of 3 m thickness the present shielding design is adequate from the point of view of the environmental impact.

From all radionuclides created in the soil ^{3}H and ^{22}Na can represent a hazard. They are in a soluble chemical form and have long $T_{1/2}$ s.

After 40 years of continuous operation in the 100 cm layer of soil surrounding the concrete wall (Volume=$1.672*10^{9}$ cm^{3}) average estimates of $5.265*10^{4}$ Bq of ^{3}H and $1.301*10^{4}$ Bq of ^{22}Na were found. If one compare these values with the generic clearance levels provided in (IAEA, 1998) of 10^{12} Bq a^{-1} ^{3}H and 10^{5} Bq a^{-1} ^{22}Na it results clearly that the level of the soil/ground water activation is much lower than the annual release constrains. The transport of the radioactive species into the ground does not represent a hazard for the population.

It should be noted that the clearance levels mentioned above were derived to assure the compliance with an annual dose to the critical group of 10 μSv y^{-1}

Nevertheless a real evaluation of the environmental impact has to be done after the site of the facility will be chosen. Results of a hydro-geological study of the construction site and site specific data will provide a realistic evaluation of the exposure pathways as well as an accurate estimation of the fraction of the ground water that might reach the public water supplies.

3 PRELIMINARY CONCEPT OF THE BEAM DUMP

3.1 Development of a concept for the beam dump

The beam dump is an essential component for the final stop of the heavy ion beam delivered by post-accelerator. The large amount of the heat and radioactivity produced in the dump at the beam interaction zone should be properly evacuated in order to provide safe and efficient operation conditions including maintenance requirements. A beam dump configuration having a fixed water-cooled graphite core with a V-shaped profile to distribute the beam along the entrance surface was investigated here and results of our studies are presented. A similar dump design is planned for the BigRIPS separator at RIKEN (Kubo, 2003) and at SuperFRS separator at GSI (Geissel et al, 2005). In this pre-conceptual design stage we took advantage of the present knowledge and experience and considered sufficient to assess the feasibility of one of these existing dump designs for our specific case and to analyse both shielding requirements and nuclear inventory.

The starting point for the interactive design process was determining the energy deposition in the dump in order to verify if for the configuration chosen the local rising of the temperature in the hot spot of the beam (Bragg peak) is tolerable. The calculated heat distribution in the dump will be further used for the thermal and stress analysis. Thermodynamics evaluations are beyond the aim of this work. A next step is necessary to analyse if dump structure have enough cooling capacity and if is able to withstand the thermal stresses induced by the heat. In addition, the radiation damage of the dump materials is an important issue that has to be estimated to check if the central part made of graphite might withstand the full beam power for a desired period of time.

Through these complex investigations the conceptual model used will be validated and developed to achieve with sufficient margin the beam power limit. In conjunction, sensitivity calculations of the residual activity varying with the size of the dump items might be carried-out to analyse the possibility to reduce the dose rates required for the development of a dump handling concept and to enable hands-on maintenance after a short waiting time.

In this context we have started the development design procedure by studying if the dump model presented in the left panel of Figure 9 is suitable to EURISOL high energy heavy ion beam conditions. This dump design was optimised at GSI (Weick, 2008) for 1300 MeV u^{-1} ^{238}U beam with a total power of 51 kW. It consists of two parts: 40 cm long graphite (absorption part) and subsequent 100 cm iron block (shielding part) with a height of 16 cm and 30 cm width. The water cooling pipes are indicated in Figure 9 as a homogenized mixture of copper with 10% of water allowing a water-free region in the transversal direction of 8 cm. The opening of the dump is ~5^o (a slope of 0.1). For graphite we considered the same carbon (density 1.84 g cm^{-3}) composition as in the case of GSI.
The beam dump for the EURISOL post-accelerator is supposed to withstand similar beam power as that one at GSI, namely the intense ^{132}Sn beam (150 MeV u^{-1}, 6.24 10^{12} pps) of the 19.8 kW power. Although the total beam power at EURISOL is smaller by more than a factor of two, the deposited energy density is comparable due to smaller incident energy and smaller beam size (σ = 2 mm of the Gaussian distribution) of the EURISOL ions.

The energy deposition in the dump was calculated using both PHITS and MCNPX2.6.e computer codes. The analysis of the obtained results shows that, in comparison with PHITS code, MCNPX gives higher energy loss in the Bragg peak and underestimates the energy deposited downstream the peak. To be in the safer side in deriving the rising of the temperature from the hot spot of the radiation heating only MCNPX energy deposition results are presented in the paper.

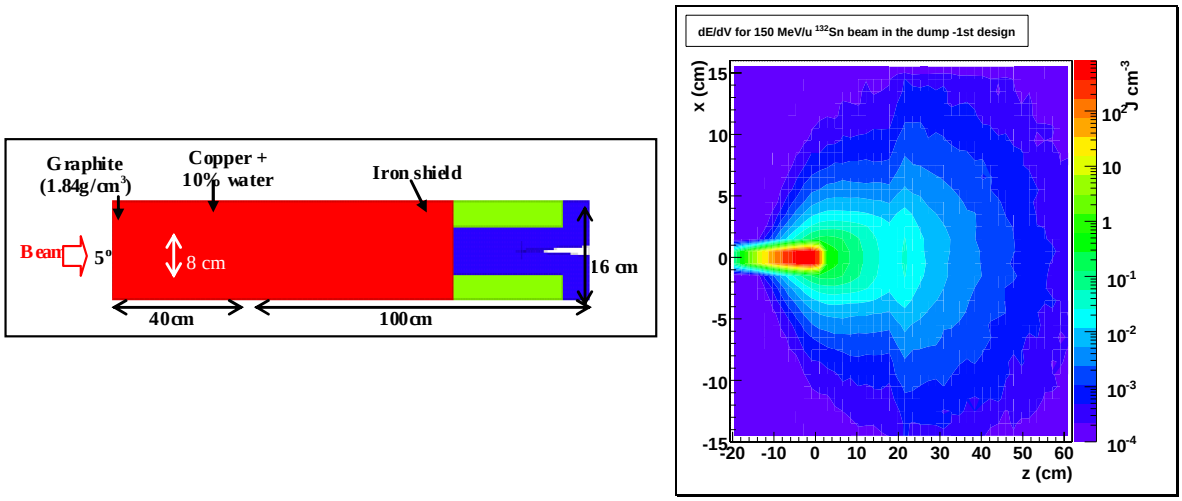

Figure 9: The geometry model of the beam dump used in simulations (left). The distribution of energy deposit per volume element in the mid-plane of the dump (right)

From two-dimensional energy deposition map presented in Figure 9 right panel as well as from Figure 10 one can see that the maximum energy deposited (Bragg peak) is about 1 kJ cm^{-3}. Considering this energy deposition adiabatic one can calculate the rising of the temperature from the temperature dependent values of the thermal capacity C, see (www.ra.anl.gov/INSP/matprop), at a given initial temperature.

For an ambient initial temperature this calculation leads to a maximum temperature rising ΔT_{max} ~ 765 K. As graphite ignites in contact with the air at around 400°C, for safety reasons the dump has to be put in vacuum or surrounded by an inert gas environment.

As the use of a higher initial temperature will slightly increase the heat capacity, the maximum instantaneous temperature rise can be reduced by changing the operation conditions. One can conclude from these conservative considerations that GSI beam catcher design might be able to accommodate the EURISIOL post-accelerator anticipated requirements.

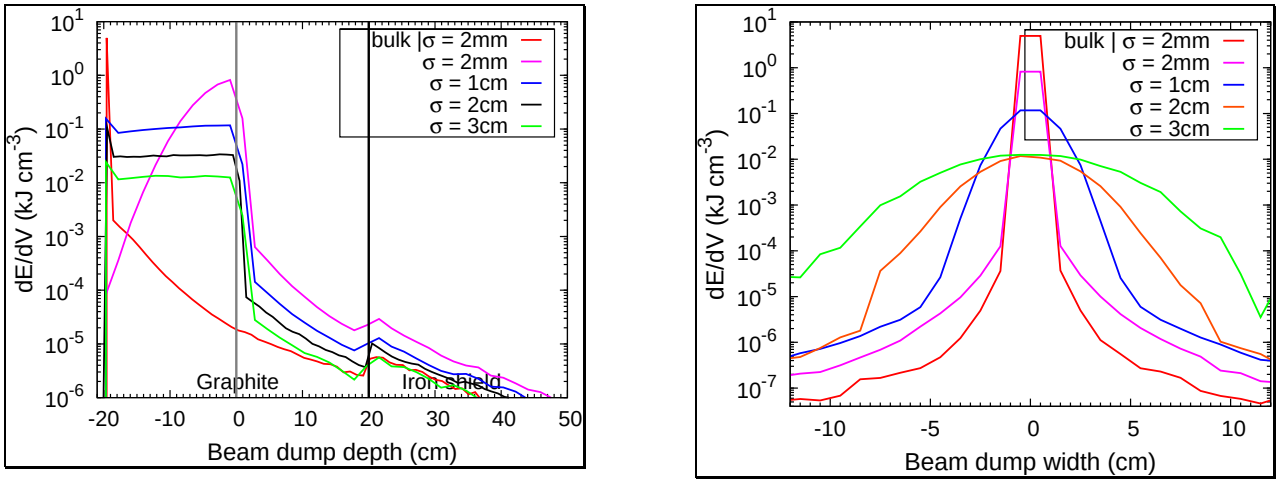

Figure 10: Variation of the beam dump energy deposition as a function of the beam size (150 MeV u^{-1} ^{132}Sn; 6.24 10^{12} pps). On the left side is presented the axial profile, while on the right panel the radial one.

In order to avoid the danger of ignition in case of the vacuum break down a possibility to reduce the maximum temperature rise by the beam dispersion might be previewed. This solution involves the use of a kicker magnet able to increase the beam size. Of course, the installation of a dedicated magnet would imply supplementary costs for the installation.

Figure 10 illustrates the beam size dispersion and the resulting decrease in the maximum absorbed energy density in the dump with the increasing of the beam size. The graph contains also the energy deposition results in case of a bulk dump in order to demonstrate the enhanced performance achieved by the geometrical shaping at the dump entrance. The Bragg peak is reached at a distance less than 1 cm in the bulk dump, what is in a good agreement with the range in carbon of this ion at 150 MeV u^{-1} i.e. 1038 mg cm^{-2} as obtained using ATIMA code, see (www-linux.gsi.de/~weick/atima).

The choice of a beam size of $\sigma \geq 1$ cm can reduce the temperature rise in the dump to comfortable values, which would not require vacuum conditions. Therefore, the beam size selection should be dictated by technical/financial considerations. As it is resulted from the machine design estimates (Normand, 2008) a magnet length of 5 m is necessary to increase the beam size to $\sigma = 1$ cm, while further increasing to $\sigma = 2$ cm will need another 4 m of the magnet length. The effectiveness of the solution proposed is pending. It should be judged by balancing the hazard and costs associated with the vacuum conditions in the dump cave versus the costs of supplementary shielding needed for the kicker magnet together with its supplementary risk. In addition, an accurate thermal study will be needed to calculate the temperature distribution in the dump in order to confirm the values obtained by simplified considerations in this work.

Another important note is worth to be mentioned. From our previous analysis (Ene, 2008) of the beam species and energies it was found that high-energy light mass ions produce higher equivalent dose rates over the concrete shield transversally to the beam direction. Therefore a dedicated study will be necessary in order to determine if for the forward direction the reference beam ^{132}Sn represents the worst case for the radiation heating problem.

3.2 Activation of the beam dump components

The magnitude of the radioactive material inventory generated at the beam dump cave represents a significant element of the overall hazard analysis of the post-accelerator facility. For activation analysis we have used the same calculation sequence described in chapter 2.2.2. PHITS coupled with the DCHAIN-SP2001 code to compute the nuclide inventory, radioactivity, decay heat and gamma-ray energy spectra and MCNPX photon transport simulations carried out further to estimate the ambient dose equivalent rates at surface and at one metre distance from the irradiated element. Compositional data of the component materials were those given in the chapter 2.2.1.1. For graphite we have used data resulted from the last analysis of a carbon target at PSI (Wohlmuther, 2008). The residual activities in the beam dump materials are presented in Figure 11. These values were obtained using 3 h of irradiation with the ^{132}Sn beam (150 MeV u^{-1}, 6.24 10^{12} pps).

We found that at the end of bombardment the highest radioactivity is arising from the copper structure elements while graphite and iron have reached total activity level of about 10^{11} Bq. After few days, the activity in the iron dump item is larger than that of the graphite due to larger number of long half-life radio-nuclides produced in the iron compared with the radioisotopes created in the graphite. In the copper part of the beam dump the total activation value of approximate 10^{8} Bq cm^{-3} at 1 hour decay time is due to ^{64,62,61,65}Cu radio-nuclides from which ^{64}Cu is the main contributor, while at longer decay times ^{59}Fe, ^{60}Co, ^{3}H and ^{63}Ni are dominant.

It is evident from the same Figure that for the graphite component, ^{3}H and ^{7}Be are of great importance. As graphite is hit directly by the primary beam one can observe in addition the reaction products originating from the projectile fragmentation. They cover an element range up to ^{132}Sn but their amount represents only few percent compared with ^{7}Be, which is the main contributor for this case.

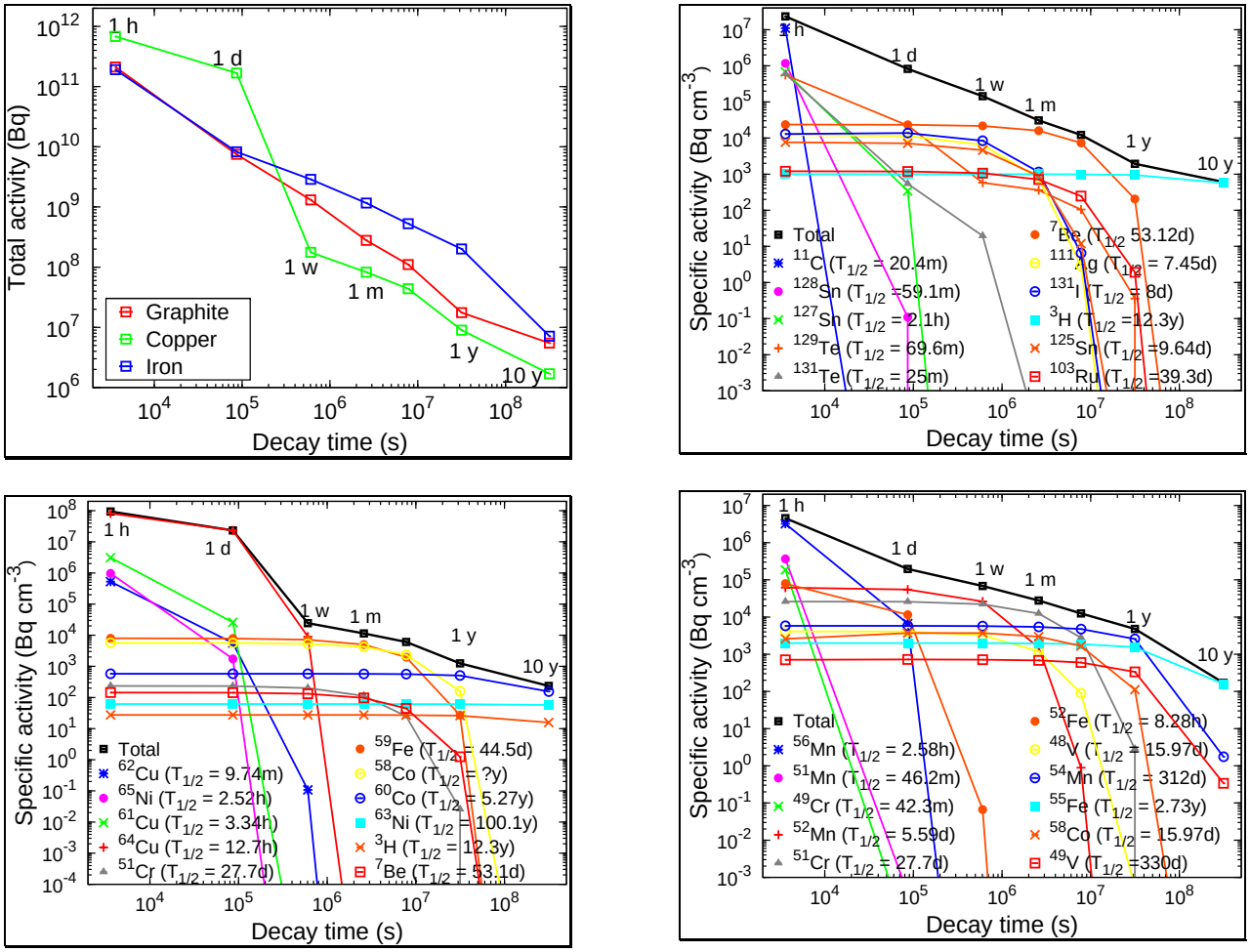

Figure 11: Obtained radioactivity distributions induced in the dump components versus the cooling time. Results correspond to the total activities (top-left) and the specific activity of the dominant radio-nuclides produced in the copper zones (top-right). On the bottom the specific activity of the produced dominant radio-nuclides corresponds to the graphite (left) and iron (right).

In the iron part of the beam dump many longed-lived radio-isotopes are produced. As seen from the same Figure, the most important ones are ^{51}Cr, ^{52}Mn, ^{54}Mn, ^{48}V, ^{49}V, ^{58}Co and ^{55}Fe. Produced volatile gas beta emitters as ^{3}H and ^{37}Ar should be mentioned as they can induce contamination all over the experimental area. The cooling water of the beam dump will be activated at about 10^{9} Bq with major contributors being ^{3}H and ^{7}Be.

The results of the calculations of the dose rate distribution for the described above configuration are presented in Figure 12. As indicated from this Figure the part directly exposed to the beam will become highly activated with dose rates one order of magnitude higher than those of the shield part. The high dose rate values are significantly higher than the allowed limits, what shows that the direct maintenance of both parts of the beam dump will be impossible

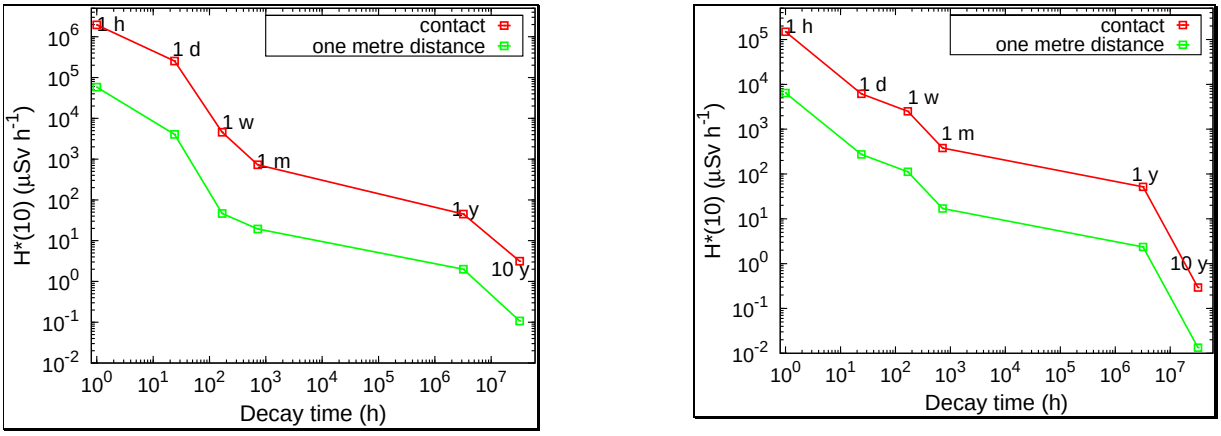

Figure 12: The resulting dose equivalent rate H(10) distributions versus the cooling time induced by the activation of the dump components: graphite and copper-core part (left) and shield part (right).*

A remote handling system will be therefore necessary to manipulate the dump devices and a hot cell might be needed in the facility lay-out. Dedicated calculations will be needed to design the required shielding of the device used to transport beam dump items to a nearby hot cell or storage place.

3.3 Shielding design for the beam dump

After some iterative simulations we conclude that additional shielding is required to reduce the high intensity of the secondary particle emission from the dump. The shielding for the beam dump needs also to be optimized to minimize the costs.

Preliminary estimates of the lateral shielding for the beam dump were carried-out in order to find the required thickness of the shielding material. The acceptable levels outside the shielding were taken the same as for tunnel shielding design (chapter 2.1.1), namely 0.1 μSv h^{-1} for public areas and 10 μSv h^{-1} for controlled areas.

PHITS simulations were performed to obtain the attenuation curves and optimum thicknesses to satisfy the shielding requirements for the two candidate materials previously analysed: ordinary concrete (ρ=2.35 g cm^{-3}) and stainless steel (ρ =7.8 g cm^{-3}). In the simulations the 19.8 kW, 150 MeV u^{-1} ^{132}Sn beam has a Gaussian profile defined by σ = 1 cm. All particles were transported with an energy threshold of 1 keV except the neutrons (down to thermal energies).

A cylindrical shield of thickness 5 m and length of 170 cm was placed at a distance of 1 m from the beam axis. The space inside the shield containing the beam dump was filled with void. Secondary neutrons and photon dose rates were scored using a virtual (10 X 10) cm cylindrical tally mesh grid

overlapping the geometry. Separate simulations for two accounted shielding materials were performed in order to estimate the required shielding wall thicknesses.

Neutron and photon dose equivalent rate maps in the iron shield of the beam dump cave are shown in Figure 13. As expected, the contribution of photons to the total dose rates is negligible showing that the neutrons are the dominant factor in the shielding estimates.

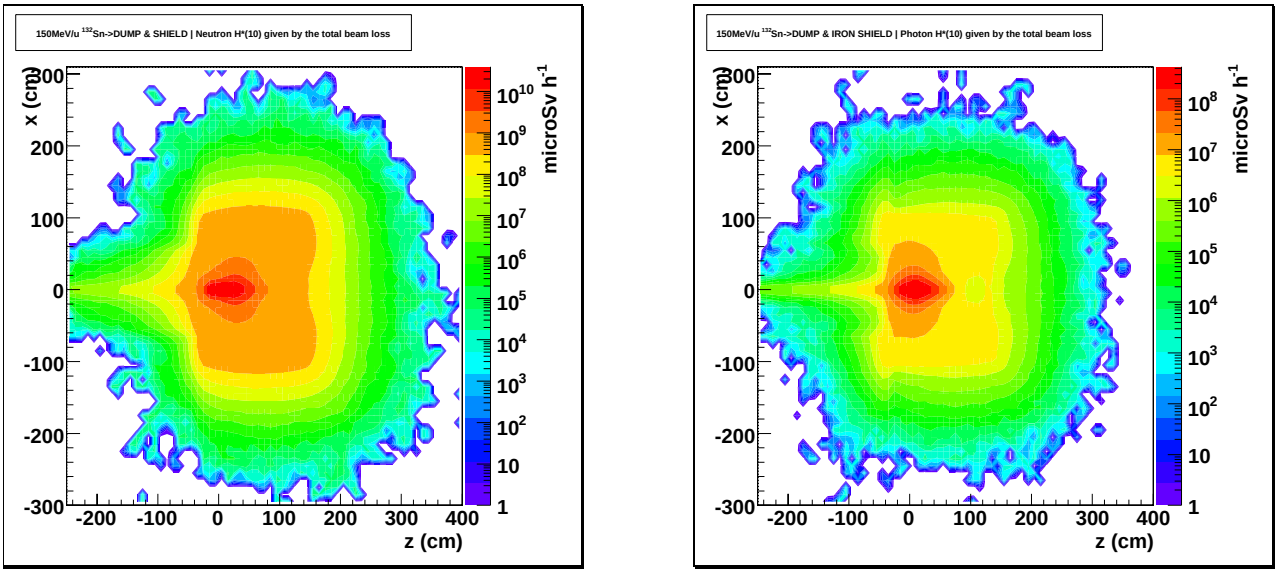

Figure 13: Estimates of the dose rate H(10) in the dump cave shielding: for neutrons (left) and photons (right).*

The axial distributions of the dose equivalent rates at several depths in the shield are biased in the forward direction showing the cascade developing. The peak laying at around 1 m from the beam impact with the dump is better observable with the thickness increasing of the shielding wall. Therefore to be on the safe side, all the results presented in this paper are referring to the axial location z ~1 m from the dump entrance. As for the tunnel the resulted neutron attenuation curve in concrete were further fitted by a double-exponential function, approach developed in (Agosteo, 2004) for transmission of secondary neutrons generated by heavy ions of intermediate energies. In contrast with the concrete, the neutron attenuation curve for iron shield after the build-up zone follows one single exponential trend. Therefore in this case the simple analytical equation recommended in (Thomas and Stevenson, 1988) was used for the fit.

The difference of the neutron dose equivalent distributions in concrete and iron may be understood observing the resulting neutron spectral fluence distributions with the shielding depths in these materials. The concrete has a “hardening effect” while the iron is “softening” the neutron spectra. We refer the reader for details presented in (Agosteo, 2008). Results of estimations and corresponding parameters from the fitted curves used to derive the required thickness of the shield walls are presented in Table 4.

Table 4: Shielding thicknesses of the beam dump cave required to reduce H(10) below the dose limits in the controlled area and public area. Source terms and mass attenuation lengths for neutrons fitted using the analytical formulation are also included.*

material	H_1 [Sv m^2]	λ_1 [g cm^{-2}]	H_2 [Sv m^2]	λ_2 [g cm^{-2}]	**Shield [cm]**	
					Staff	**Public**
concrete	1.747E+3	23.7	1.338E+2	60.36	**364**	**480**
iron			5.000E+4	112.14	**254**	**320**

In order to reduce the thickness of the shielding wall the analysis of an optimum combination of these shielding materials will be necessary.

4 EXPERIMENTAL HALL

The purpose of this study is to configure the shielding and the management of the access to the controlled areas inside the beam experimental halls.

4.1 Calculation method

In agreement with requirements of the physics case of the project, see (Page, 2008), it was decided to investigate six target materials: CH_2, Be, C, Cu, Ni and Pb at two possible thicknesses of 1 mg cm^{-2} and 10 mg cm^{-2}.

Table 5 summarizes the characteristics of the experimental hall area agreed together with the Task#10 "Physics and Instruments" and used here in simulations.

The experimental hall hosting the AGATA germanium array detector was selected in agreement with (Page, 2008) as being the conservative case. Therefore the corresponding room size (see the Table 5) accounts for the magnetic spectrometer coupled with the detector.

A simplified geometry was used to model the mounting frame of the detector clusters. Thus a germanium spherical crown with thickness of 10 cm and internal radius of 25 cm lined internally with 3 mm of aluminum sheet was assumed in the model. A beam drive tube with 6 cm opening and an exit tube of 16 cm diameter complete the detector scheme used in simulations. A fictitious cutting through the Ge detector model delimited by a cone with an opening of 30^o was done also in order to account separately for the contribution of the forward zone of the detector to the activation.

The conceptual model for the beam dump system to be placed at the end of the post-accelerator beam line, (see chapter. 3) was used here also to examine safe operation conditions inside the experimental areas. A slight change was nevertheless accounted. For comparison reasons in the model it was kept the same aperture angle of the opening but was considered a conic shape for the active beam dump (ADc) inside the experimental hall instead of the wedge shape opening of the passive dump (PDw) placed at the end of the accelerator.

Therefore the geometry model used in simulations contains a) a simplified AGATA detector placed in the centre, b) a typical experimental target positioned inside AGATA, and c) a conic-shaped beam dump configuration with a water-cooled graphite core and a subsequent iron block downstream of the beam line, placed at 2 m downstream to the target.

An operation scenario of twelve days campaign with subsequent cooling times up to 10 years was used for estimations. A test case of $^{132}Sn^{25+}$ RIB at 150 MeV u^{-1} was used in simulations.

Neutron production yields from the physics targets, dose rate estimates in the experimental area and behind the shielding walls and energy deposition on the beam dump were calculated by means of the PHITS Monte Carlo computer code.

In order to characterize the residual radiation environment inside the experimental halls the established procedure (chapter 2.2.2) was used. Induced radioactivity in the targets, AGATA equipment, concrete wall and the air inside were estimated using DCHAIN-SP-2001 code. The lay-out of the experimental area was schematically configured by preliminary sizing of concrete shielding walls. The magnitude of the radioactive material inventory generated inside this zone and the associate dose rate estimates were determined. Further investigation of the preliminary concept of the experimental area will be necessary.

Table 5: Characteristics of experimental hall
of EURISOL postaccelerator needed for shielding & safety estimates

Beam characteristics			**Target characteristics**			**Room characteristics**		
Heavy ion	**Energy [MeV/u]**	**Intensity [ion s^{-1}]**	**Physics target**		**Dump Material**	**Size [m x m x m]**	**Content**	**Equipment**
			Material	**Thickness [mg cm^{-2}]**				
$^{132}Sn^{25+}$	21, 150	6.25 10^{12}	Be, C, Ni, Cu, Pb, CH_2	1-10	C	40 x 20 x 10	air	AGATA type*

*- conservative simplified geometry

Operation scenario: 12 days of irradiation with subsequent different cooling time

4.2 Results and discussion

4.2.1 Selection of the representative experimental target

Results of experiment targets investigation are presented in the Table 6 and Figs 14-15.

The table shows clearly that the maximum total production yield arises from the Beryllium target.

Table 6: Total neutron production yields resulted from calculations

	1 mg cm^{-2}	10 mg cm^{-2}	
Nuclide	**Neutrons ion^{-1}**	**Neutrons ion^{-1}**	**thickness(cm)**
Be	2.7098E-03	2.6065E-02	5.4110E-03
CH_2	2.5092E-03	2.4060E-02	1.0420E-02
C	2.3942E-03	2.2532E-02	4.4110E-03
Cu	1.7993E-03	1.4897E-02	1.1210E-03
Ni	1.7822E-03	1.4429E-02	1.1230E-03
Pb	1.5018E-03	1.3177E-02	8.8180E-04

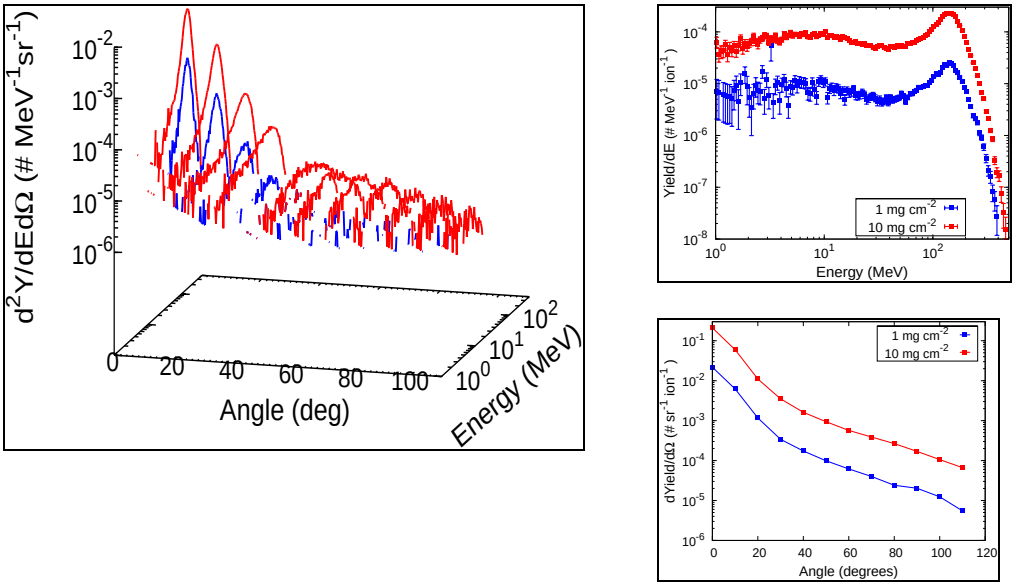

Figure 14 Neutron production yields comparison for Be target (1mg cm^{-2} vs 10 mg cm-^{2}): on right is represented double differential energy angle distribution and on left: energy distribution (top) and angle distribution (bottom)

Note also the small difference in the total neutron yields occurring between first three target materials as well as between Cu and Ni materials from the Table.

As expected the most conservative cases are given by the targets of 10 mg cm^{-2}. The differences of the resulted neutron yields distributions for Be material at the two thicknesses accounted are illustrated in the Fig. 14. One can see clearly that the neutron yield results reflect the difference in the thickness of the targets.

Detailed analysis of the neutron yields distributions for 10 mg cm^{-2} case presented in the Fig. 15 shows that the Be results are superior to others at high energy and forward directions while at low energy and large angles the conservative case is Pb material.

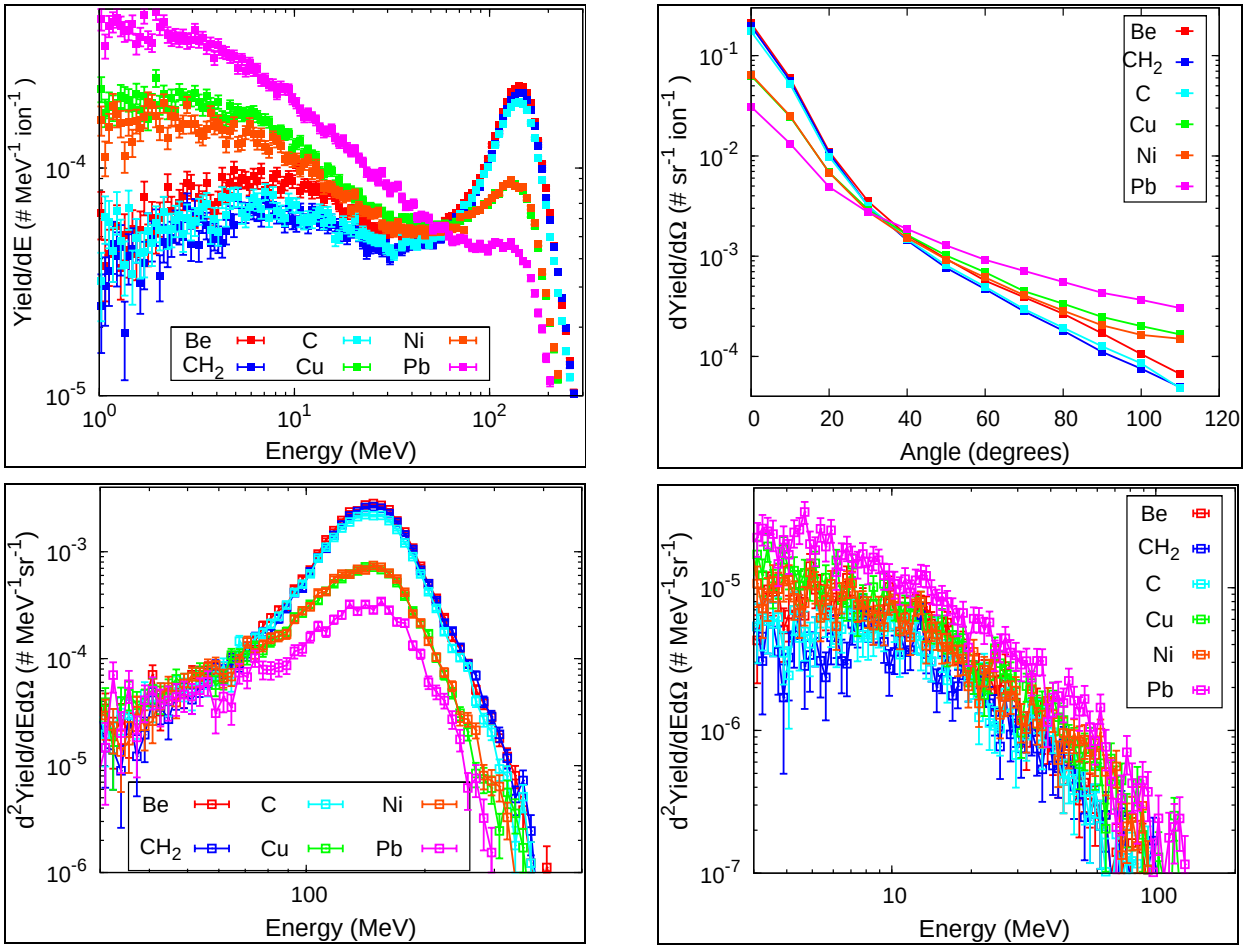

Figure 15: Neutron production yields for the target materials accounted: top right, the energy distribution, top left, the angular distribution, bottom, the energy distribution for forward direction (left) and on the perpendicular direction relative to beam axis (right). For all graphs the 10 mg cm^{-2} case is presented.

The graph reveals also the strong forward biasing of the yield results (more than 3 orders of magnitude difference).

One can conclude from this study that the target of Be material having 10 mg cm^{-2} thickness represents the most penalizing case and it will be used for further investigations.

4.2.2 Prompt field

The use of the penalizing target configuration in the computational model described in the chapter 4.1 got the H*(10) results presented in the Fig. 16. The right panel of the Fig.16 presents the radial distribution of the H*(10) resulted from this calculation in comparison with the similar radial distribution derived from Fig. 13. For both distributions depicted in the graph it has been chosen the axial locations that give the maxima of the cascade developing (indicated with 'forward' direction in the right side of the Fig. 16). The analysis of the compared distributions in

the Fig. 16 leads to the conclusion that at the beam dump exit the H*(10) results are almost at the same levels. The difference occurring outside the beam dump is due to the air attenuation for the experimental hall case. Note also that for the PD cavity the shielding wall was placed 1 m from the beam axis (see chapter. 3.3). Obviously the preliminary concept of the AD used here should be further checked and developed via thermo hydraulics complex studies.

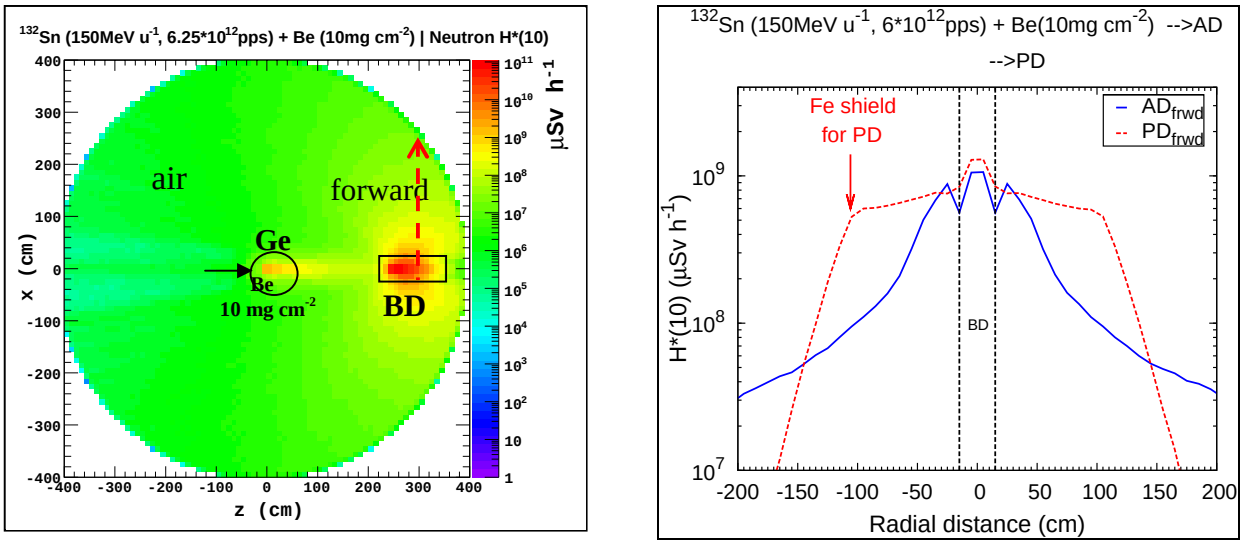

Figure 16: Derived H(10) for the experimental set-up: left the distribution in the mid-plane and right the comparison of the radial profiles. ADc is the active dump with conic opening and PDw is the passive dump with wedge opening (see Fig.13).*

Therefore for a rough, conservative approximation one can conclude that the shielding thickness derived for the PD cavity (see Table 4) might be used also for the walls of the experimental hall hosting AGATA detector. Further analysis of the energy deposited in the AD and the derived axial profile compared with that obtained for PD supplied in the Fig. 17 corroborates the above conclusion.

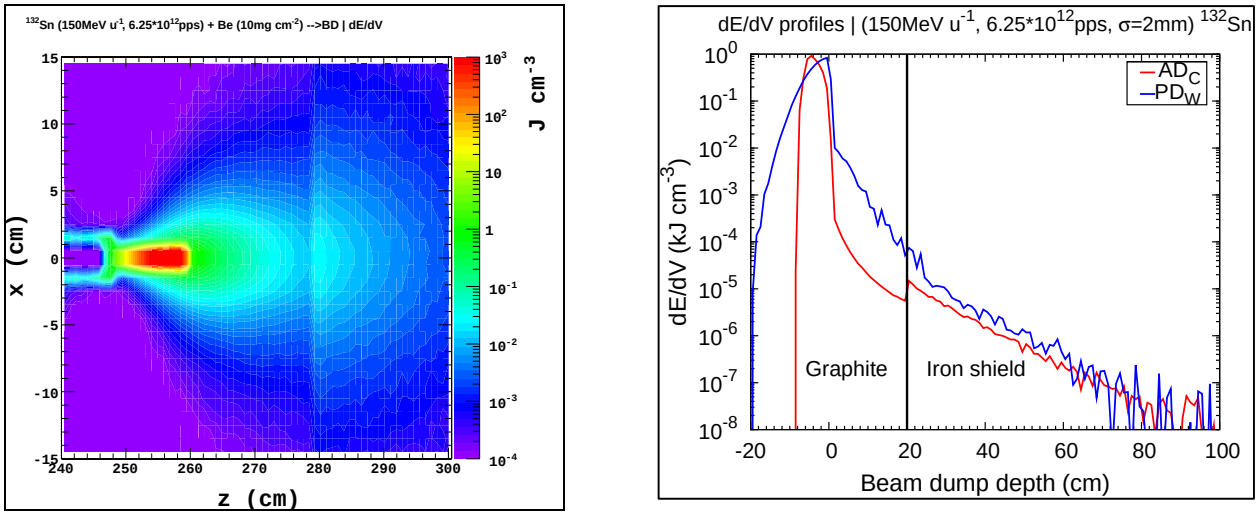

Figure 17: The energy deposition per volume element: (left) distribution in the mid-plane of the active dump and (right) the comparison of the axial profiles. ADc is the active dump with conic opening and PDw is the passive dump with wedge opening (see Fig. 9)

The obtained results have demonstrated that the detailed model of the experimental hall is not necessary to be done explicitly and that the simplified model used for the experimental set-up used in calculations is enough to justify the rough derivation of the shielding issues based on the previous results.

4.2.3 Residual field

Results of the activation calculations performed using the simplified model are presented in the Fig. 18. The left side of the figure shows the induced specific activity for Germanium detector forward zone. At the beam shut-down moment the main contributors to the activation concentration are isotopes of ^{72}Ga, ^{73m}Ge, ^{70}Ga, ^{73}Ga, ^{69}Ge, ^{71}Ge. For cooling times beyond one week until one month ^{71}Ge gives dominant contribution, while for longer time intervals ^{68}Ga and further ^{3}H are the most important ones.

Consequently to the large activation values found the estimates of the associated H*(10) are by far taken over the staff limit of 10 μSv h^{-1}. Even the minima of the H*(10) results placed on the backward region of the Ge detector are much higher than the staff limit that shows that the 'hands-on' manipulation of the detector will be not possible even after more than one week.

One can conclude from this study that the use of the AGATA array detector at the maximum ^{132}Sn intensity of 10^{13} pps corresponding to the energy of 150 MeV u^{-1} will not be possible. The obtained results have been discussed with AGATA developers, that certified that indeed the use of this detector is prohibited at the levels of the secondary neutron flux arising from 10^{13} pps ^{132}Sn interaction at 150 MeV u^{-1} with target materials, see (Theisen, 2009).

Further studies have to be devoted to other detector set-ups able to measure secondary fluxes arising from heavy ion interactions at the high energy delivered by the EURISOL facility.

The level of air activation around the beam dump after twelve days of beam-on and various times of beam-off until one year is given in Fig. 18 right panel. This graph shows the high level of the air activation (see discussion in the chapter 2.3.2) that will require carefully analysis for ventilation rate assessment.

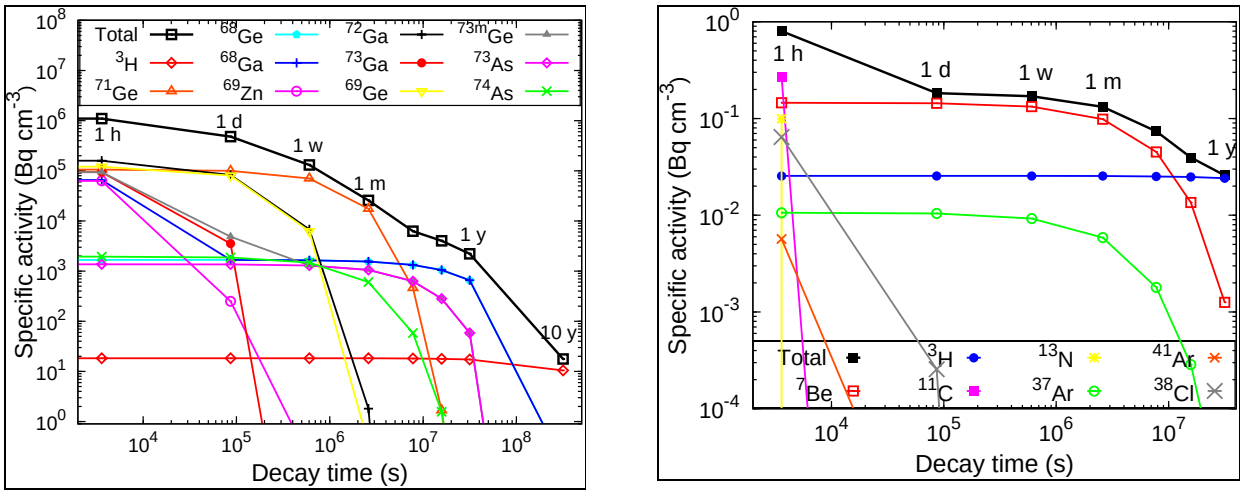

Figure 18: Results of the radioactivity versus the cooling time: (left) the total specific activity and the dominant radio-nuclides produced in the Ge detector (forward zone) and (right) the total specific activity and the dominant radio-nuclides produced in the air

5 CONCLUSIONS

This work is the first radiological study of the EURISOL post-accelerator, which is one of the key issues in the safety design of the entire EURISOL facility.

Initial facility radiation field simulations were carried-out to obtain radioactive doses and levels of activation. These estimations are very important to identify the main radiological issues and find out possible solutions.

In this work it has been demonstrated that PHITS/JQMD and MCNPX/LAQGSM are appropriate tools to evaluate the transmission of secondary neutrons arising from heavy-ion interactions in incident intermediate-energy range. Both physics models used show an overall good agreement with the experimental data. In addition, the two codes give comparable results for our reference reaction except for the energy deposition simulations, where MCNPX provides lower values in the region over the Bragg peak.

Both prompt and residual dose estimates were performed providing the approximate size/volumes of the Linac building and resulting radioactivity inventory of the activated structures including air and soil activation. Through the analysis of the obtained results the shielding walls of the accelerator tunnel have been sized. Estimates of the activated materials around the beam loss for two accelerator energy zones give useful information regarding the maintenance and intervention operations.

In addition, a pre-conceptual model for the beam dump system to be placed at the end of the post-accelerator beam line has been developed. Results of investigations have demonstrated the feasibility of this model to absorb high heat loads of the primary beam and resulting high radioactivity.

The lay-out of the beam dump facility was schematically configured by preliminary sizing of the shielding walls and analyzing the possibility to use a kicker magnet that will allow safety operation conditions. Nevertheless, a detailed thermo-hydraulic analysis is still required to examine the temperature and stress distributions and to address the design of the dump cooling.

The work was finally complemented with the characterization of the experimental area by using a simplified experimental set-up based on AGATA array detector.

We note in view of our findings described above the large values of activation levels in the Germanium detector that makes it inadequate at the maximum delivered ^{132}Sn beam intensity of 10^{13} pps .

In conclusion progress has been done towards understanding the spatial distribution of the dose relative to accelerator components, the beam dump and the adjacent experimental hall and the level of resulting residual field.

The preliminary analyses accomplished here were driven to answer to the relevant questions for the post accelerator area radioprotection problems. As has been discussed above, due to the conservative assumptions and primary data used, these studies have led to conservative results.

However, the obtained results will provide baseline for detailed studies which will be mandatory to be performed in a second iteration for a more advanced design stage.

The obtained results will serve to estimate the entire costs of the facility having a strong impact on the decision and the strategy to be adopted as long as safety and radioprotection issues are concerned.

4. Acknowledgements

We acknowledge the financial support of the EC under the FP6 "Research Infrastructure Action - Structuring the European Research Area" EURISOL DS Project; Contract No. 515768 RIDS; www.eurisol.org. The EC is not liable for any use that may be made of the information contained herein.

REFERENCE

EURISOL Design Study, http://www.eurisol.org

International Nuclear Safety Centre, Materials and Properties Database, "Recommended Graphite, Enthalpy Increments and Heat Capacities", Argonne Nat. Lab./US-DOE Internet documentation, http://www.ra.anl.gov/INSP/matprop.

http://www-linux.gsi.de/~weick/atima.

10 CFR Appendix A to Part 835 - Derived Air Concentrations (DAC) for Controlling Radiation Exposure to Workers at DOE Facilities, http://cfr.vlex.com/vid/835-concentrations-dac-controlling-19618720

International Commission on Radiological Protection Recommendations, ICRP Publication 60, 1990, (Oxford: Pergamon Press)

Aubert, F.,. Inventaire et Compositions Chimique des Matériaux du Réacteur ULYSSE de Saclay, CEA DAPNIA/ SENAC/E/05-193/NT.. Inventaire et Compositions Chimique des Matériaux du Réacteur ULYSSE de Saclay, CEA DAPNIA/ SENAC/E/05-193/NT, (2005)

Agosteo, S, Silari, M., Preliminary shielding calculations for a 2 GeV superconducting proton Linac. Technical report: TIS-RP/TM/2001-028, CERN , (2001).

Agosteo, S, Nakamura, T., et al, Attenuation curves in concrete of neutrons from 100 to 400 MeV per nucleon He, C, Ne, Ar, Fe and Xe ions on various targets, NIM/B 217, 221, (2004).

Agosteo, S, et al. "Shielding data for 100-250MeV proton accelerators: attenuation of secondary radiation in thick iron and concrete/iron shields", NIMB 55782, to be published, (2008).

Ene, D, et al., "Preliminary Shielding Assessment of the EURISOL Post-accelerator", presented at ICRS-11 - 11th International Conference on Radiation Shielding, and RPSD-2008 - the 15th Topical Meeting of the Radiation Protection and Shielding Division of American Nuclear Society, April 13 - 18, 2008, Callaway Gardens, Pine Mountain, Georgia, USA; to be published in *Nuclear Technology*.

Fasso, A., et al., 1990, Shielding against high energy radiation, Numerical data and functional relationships in science and technology, Vol. 11, Ed. H. Shopper, Springer-Verlag, Berlin.

Furihata, S. et al, GEM-code –A simulation program for the evaporation and fission process, JAERI-Data Code, 2001-015, JAERI, Tokaimura, Japan, (2001).

Geissel et al., Technical Report on the Design, Construction, Commissioning and Operation of the Super-FRS of FAIR, (2005)

Kay T., Maekawa F., Kosako K., et al, 2001. DCHAIN-SP 2001: High Energy Induced Radioactivity Calculation Code, JAERI- Data Code 2001-016 (in Japanese), (2001).

Kubo, T., NIMB 204, pp. 97 (2003).

IAEA, Clearance of materials resulting from the use of radionuclides in medicine, industry and research, IAEA TECDOC-1000, Vienna, (1998)

Iwase, H., Niita, K., Nakamura, T., J. Nucl. Sci. Technol. 39(11), 1142, (2002)

James, M, et al., "Recent enhancements in MCNPX: Heavy-ion transport and the LAQGSM physics model, NIMA 562, pp819, (2006).

Nakamura, T., and Heilbronn, L. "Handbook on Secondary Particle Production and Transport by High Energy Heavy Ions" World Scientific Publishing Co., (2006).

Normand, G., (GANIL, French) private communication (2008).

Page, R., (Liverpool University) private communication (2008).

Ridikas et al., "High power operation of EURISOL: MMW target station and related safety issues", Proceedings of the 8th International Topical Meeting on Nuclear Applications and Utilization of Accelerators (AccApp'07), Pocatello, Idaho, USA, 30/07/-02/08/(2007)

Satoh, D. et al., "Re-evaluation of secondary neutron spectra from thick targets upon heavy-ion bombardment, NIMA 583, pp507 (2007).

Schlogl B., Nabbi R., Moormann R., 2007. "Calculation of the Activity Inventory of Transportable Radionuclides in Soil and Groundwater for Large Neutron Sources", EURISOL DS/Task5/TN-07-01.

Sullivan, A., H., A Guide to Radiation and Radioactivity Levels Near High Energy Particle Accelerators, Nuclear Technology Publishing Ashford, TN23 1JW England, (1992)

Thomas R. H., Stevenson, G. R, Radiological safety aspects of proton accelerators. Technical Reports Series No. 283, Vienna, IAEA, (1988).

Theisen, C., (CEA, France) private communication (2009).

Weick, H., (GSI, Germany) private communication (2008).

Wohlmuther, M., (PSI, Switzerland) private communication (2008).

Annex 1

Benchmarking the modelling tools

Neutrons produced from heavy ions interactions are the main radiation source in the accelerator shielding calculations. Physics models used in the radiation transport codes are an important factor which decides the accuracy of the simulations performed. Therefore, in order to build the confidence in the transport simulations, in this paper we have realised a comparative analysis of the physics models used. The neutron production cross sections from heavy-ion induced reactions were chosen as an observable to be benchmarked.

The PHITS Monte Carlo code uses an intra-nuclear cascade model to simulate nucleon-induced reactions and a model based on QMD (Quantum Molecular Dynamics) theory for reactions induced by both nucleons and heavy ions. Statistical decay of compound nucleus is calculated with the GEM (Furihata et al., 2001) evaporation model. Two benchmark studies (RIKEN and HIMAC) against available experimental data (Nakamura and Heilbronn, 2006) were performed initially in order to verify the accurate description of the reaction models used in PHITS code and to choose the best options to be used for the present work requirements.

The recent implementation of Los Alamos version of the QGSM (Quark-Gluon String Model) in the last variant of MCNPX code (James et al., 2006) was additionally considered in the comparisons as possible tool to handle the heavy-ion physics. Neutron double-differential cross sections from reactions induced by ^{40}Ar at two incident energies, namely 95 and 560 MeV u^{-1} were calculated using PHITS1.94 and MCNPX2.6.e codes and compared with the measurements described in the benchmarks.

The predictions of both codes tested against measured data are presented in the Figure A1. In brief, there is a reasonable agreement with the measured neutron spectra although different models show some deviations from the experimental data at different neutron energy regions (see Fig. A1). As a general trend PHITS overestimates the experiment data at lower neutron energies, while both codes reproduce rather well high energy part of the neutron energy spectra.

Both computer code estimates agree well with experimental data at large angles, while for small angles non-negligible discrepancies are observed. The biggest discrepancies are seen for the forward spectra especially at low energy, where both models failed even though for the HIMAC test problem MCNPX gives a quite good representation.

Additional comparison of the two available physics models was done for ^{132}Sn 150 MeV u^{-1} incident on a copper target, used as reference in our simulations. The resulted neutron double differential cross sections are presented in the left panel of Figure A2.

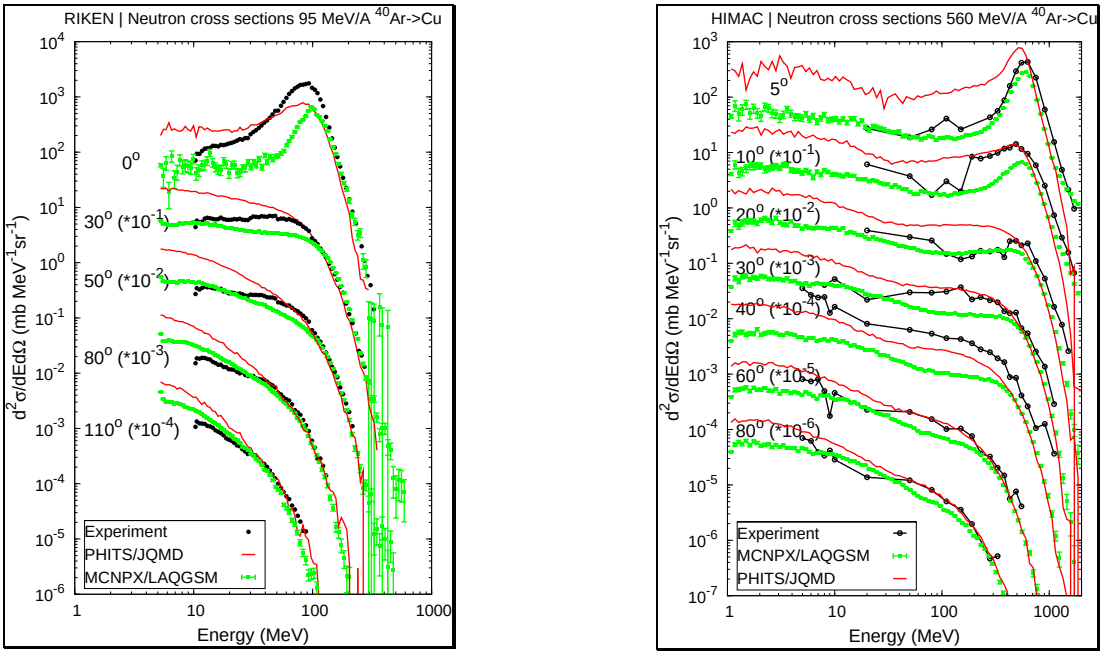

Figure A1. Comparison of the measured double differential cross sections of neutrons at 95 MeV u^{-1} (on left) and at 560 MeV u^{-1} (on right) ^{40}Ar impinging on a copper target with PHITS/JQMD and MCNPX/LAQGSM results.

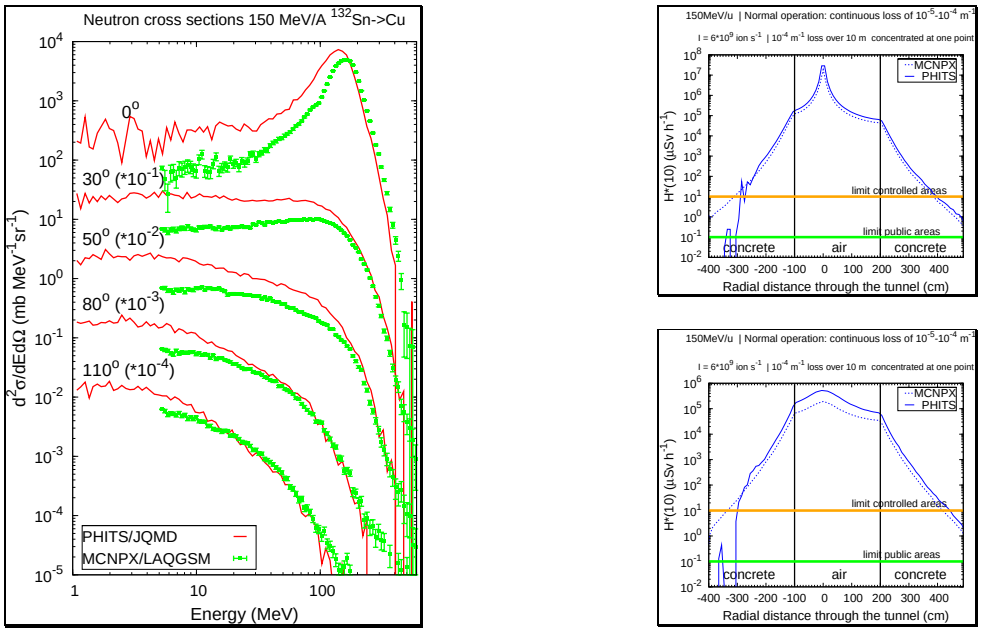

Figure A2. Two code comparison in the case of ^{132}Sn at 150 MeV u^{-1} incident on a copper target. Left: neutron double differential cross sections; Right: neutron dose rate attenuation curves in concrete wall of the linac tunnel during routine operation, where the results correspond to the beam impact position (above) and at 3 m from the beam impact (below).

On the right side of Figure A2 we show the neutron dose rate attenuation curves in concrete wall of the post-accelerator tunnel during routine operation derived using the method formulated in the chapter.2. MCNPX estimates of these curves were added in the graphs for comparison purposes. The results displayed correspond to the beam impact position in the tunnel model (above) and at 3 m from the beam impact (below)**.**

The left panel of the graph clearly shows a good agreement of the neutron spectra predictions at large angles (80^0 to 110^0) which is reflected upon the neutron attenuation curve estimates in the tunnel shield perpendicularly to the beam direction. In the central plan of the tunnel the predictions almost coincide. At small angles the agreement is somewhat worse and this is evident also from the attenuation curves comparison where the difference between codes reaches a factor 2.

We conclude at this point the good capability of the PHITS code to predict neutron spectra from thick targets bombarded with heavy ions in the intermediate range energy as was also recently demonstrated in (Satoh, 2007). All obtained results indicate that both PHITS/JQMD and MCNPX/LAQGS models are able to give a proper evaluation of the secondary neutron spectrum produced in a medium by heavy-ion bombardments within the energy range of interest around 100 MeV u^{-1}.